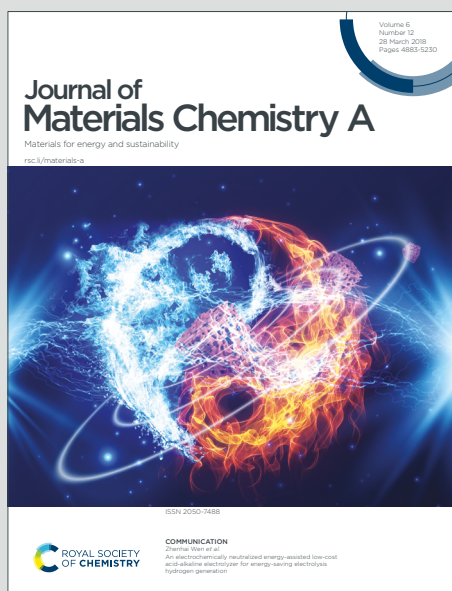


# Journal of Materials Chemistry A

Materials for energy and sustainability

Accepted Manuscript

This article can be cited before page numbers have been issued, to do this please use: Z. Xu, Z. Li, Y. Jiang, G. Xu, M. Zhu, W. Law, K. Yong, Y. Wang, C. YANG, B. Dong and F. Xing, *J. Mater. Chem. A*, 2020, DOI: 10.1039/D0TA08869B.



This is an Accepted Manuscript, which has been through the Royal Society of Chemistry peer review process and has been accepted for publication.

Accepted Manuscripts are published online shortly after acceptance, before technical editing, formatting and proof reading. Using this free service, authors can make their results available to the community, in citable form, before we publish the edited article. We will replace this Accepted Manuscript with the edited and formatted Advance Article as soon as it is available.

You can find more information about Accepted Manuscripts in the [Information for Authors](#).

Please note that technical editing may introduce minor changes to the text and/or graphics, which may alter content. The journal's standard [Terms & Conditions](#) and the [Ethical guidelines](#) still apply. In no event shall the Royal Society of Chemistry be held responsible for any errors or omissions in this Accepted Manuscript or any consequences arising from the use of any information it contains.

## ARTICLE

## Recent Advances in Solar-driven Evaporation System

Zhourui Xu,<sup>a,e</sup> Zida Li,<sup>a</sup> Yihang Jiang,<sup>a</sup> Gaixia Xu,<sup>a</sup> Mingwei Zhu,<sup>b</sup> Wing-Cheung Law,<sup>c</sup> Ken-Tye Yong,<sup>d</sup> Yanshuai Wang,<sup>e</sup> Chengbin Yang,<sup>a</sup> Biqin Dong,<sup>e</sup> Feng Xing<sup>\*e</sup>Received 00th January 20xx,  
Accepted 00th January 20xx

DOI: 10.1039/x0xx00000x

Nowadays, energy and environment have become the critical issues to determine the sustainability of the Earth. Freshwater crises, as a increasingly serious global problem, poses a great threat to our economies, environment and us. Solar-driven evaporation has emerged as a promising and sustainable approach to convert solar energy into clean water. In fact, the production of freshwater is not only governed by the heat generation at the interface, but also the process relying on the coordination and cooperation of functional modules in the solar-driven evaporation system. This review begins with system designs of solar evaporator, considering thermal manipulating structures, water transportation pathways, and vapour condensation module, which focus on improving the overall energy utilization, long-term usability, and freshwater yield. It is followed by the summary and discussions of cutting-edge solar evaporation applications and their underlying mechanisms. Finally, existing challenges and potential solutions for future applications are discussed and provided. This review aims to provide useful guidelines and references to scientists and researchers for the future development of clean water generation system.

## 1. Introduction

With the ever-growing population in the Earth within the past century, water scarcity has become one of the major threats to human society.<sup>1</sup> In this age, nearly two-thirds of the world's population live under the shadow of water shortage.<sup>2, 3</sup> In recent decades, huge efforts have been devoted to developing efficient and reliable methods to tackle water scarcity issues. However, the existing technologies which applied for large scale water supply were invented at the expense of aggravating energy problems<sup>4-6</sup> or, even worse, overly exploiting the environment,<sup>4, 7</sup> which certainly not long-term solutions. Therefore, sustainable and economical technologies for freshwater production are urgently needed.

Solar-driven vapor generation, which utilizes sunlight as the energy source to accelerate the vapor production from the sea, is a promising approach to alleviate the severe situation of water scarcity with minimum environment impacts.<sup>8</sup> Within the past decade, the strategy of solar vapor generation has undergone a rapid evolution from the volumetric configuration,

<sup>9, 10</sup> in which the photothermal agents are suspended or dispersed in water to thermalize the bulk water, to the interfacial configuration, in which solar evaporators float at the air-water interface to achieve localized heating, with increasing understanding of thermal utilization. Compared with the volumetric heating, the interfacial heating actively confines thermal energy at the water surface, reduces the heat loss to the bulk water, resulted in enhanced water evaporation rate. In addition, the facile preparation,<sup>11</sup> automatic operation,<sup>12</sup> and low capital investment<sup>13,14</sup> features of solar-driven evaporation endow great potential to be deployed especially in off-grid and remote areas. In the view of its advantages, great efforts have been devoted by scientists in the past few years to developing interfacial-based solar evaporator with the ultimate goal of freshwater production.

Although huge progress in the field of solar evaporation has been made, from the practical point of view, the current solar evaporators are still suffered from immature energy and water manipulation, resulted in unsatisfactory freshwater productivity. The basic concept behind solar vapor generation involved with several sub-processes, including optical and thermal energy utilization,<sup>15,16</sup> water transportation,<sup>17,18</sup> vapor manipulation<sup>19,20</sup> and water collection.<sup>21,22</sup> In the early stage of solar evaporation, scientists have paid much attention to photothermal materials to pursue the intensified interfacial evaporation.<sup>23,24</sup> However, the production of distilled water is not only governed by the heat generation at the interface, but also relies on the coordination and cooperation of each functional components in the solar evaporation system. A typical structure of solar evaporation system for freshwater

<sup>a</sup> Guangdong Key Laboratory for Biomedical Measurements and Ultrasound Imaging, School of Biomedical Engineering, Shenzhen University Health Science Center, Shenzhen, 518060, China

<sup>b</sup> National Laboratory of Solid State Microstructures & College of Engineering and Applied Sciences, Nanjing University, Nanjing 210093, China

<sup>c</sup> Department of Industrial and Systems Engineering, The Hong Kong Polytechnic University, 11 Yuk Choi Road, Kowloon, Hong Kong, China

<sup>d</sup> School of Electrical & Electronic Engineering, Nanyang Technological University, Singapore, 639798

<sup>e</sup> Guangdong Provincial Key Laboratory of Durability for Marine Civil Engineering, College of Civil and Transportation Engineering, Shenzhen University, Shenzhen 518060, China. xingf@szu.edu.cn

production is illustrated in Figure 1. Recent advances in this field shifted to the system designs of functional modules, including thermal manipulating structures,<sup>25</sup> water transportation pathways,<sup>11</sup> and vapor condensation system,<sup>26</sup> which aimed to tackle the problems of energy dissipation,<sup>27</sup> salt crystallization,<sup>28, 29</sup> and water yield<sup>26</sup> occurred in the solar evaporation process. These developments significantly promote the performance of solar distillation in different angles and thus maturing this green technology to a new stage.

To date, many reviews related to the solar absorbing materials and specific applications have been reported. For example, reviews reported by Gao et al.<sup>30, 31</sup> mainly focus on the investigation of photothermal materials and the system designs for energy manipulation. The review reported by Dao et al.<sup>32</sup> only describes the recent advances of carbon-based sunlight absorber for solar-driven evaporation system. Zhang et al.<sup>33</sup> presented a comprehensive review on photothermal-assisted applications including distillation, sewage treatment, photocatalysis, and water harvesting from air. Liu et al.<sup>34</sup> summarized and analysed the critical processes involved in solar desalination system with mathematical models, however without the consideration of freshwater production. Comprehensive reviews considering the whole process of solar-driven evaporation have been published.<sup>35,36</sup> Nevertheless, these reviews have been mainly focused on photothermal effects and the system structure architecture of solar-driven evaporation system was not sufficiently discussed. Given the recent reported advancements of system designs contributed to efficient energy harnessing, salt rejection, and water harvesting, it is thus time to systematically summarize the pros and cons of the technologies and map out the guidelines for supporting the future development of clean water generation system. Herein, we present the mathematical model to quantitatively evaluate the system performance of solar distillation at different stages at first. Then, we demonstrate the significance and effects of energy input, water transportation, and vapor manipulation on the performance enhancement of individual stage in solar distillation. Next, we summarize the recent progress of applications based on solar-driven evaporation and discuss the underlying mechanism. Finally, conclusion and remaining challenges in this field are presented.

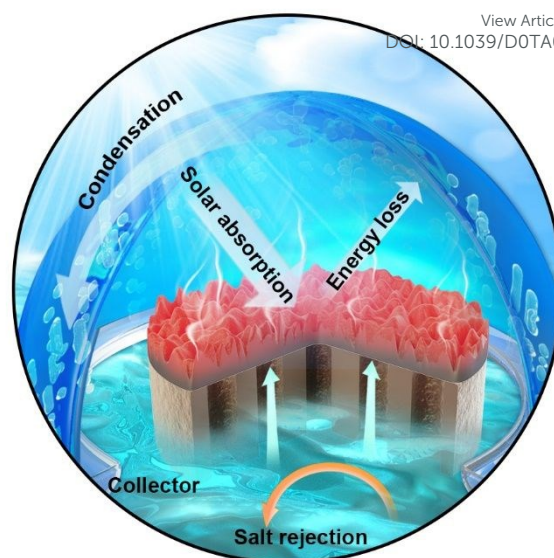


Figure 1 Schematic of the solar evaporation system.

## 2. Performance Evaluation and Calculation

A solar-driven evaporation system aims to produce freshwater using solar energy. In this process, the system firstly takes in solar energy, and then converts it into heat to vaporize water, followed by freshwater generation by condensation. Any stage in this process involves rather complex physical phenomena and energy changes. In short, the energy conversion and vapor generation mainly happen around the solar absorber, where the air-water interface locates. Taking a control volume enclosing the solar absorber, as shown in Figure 2, and assuming a steady state, there are three major energy flows, namely solar radiation, and heat loss, mass flow of water/vapor, the three of which must remain in balance. Several metrics, including photothermal conversion efficiency, solar-to-steam efficiency, and water evaporation rate, have been proposed to evaluate the efficiency of energy utilization in different stages. Efforts have been constantly devoted to improving the performance by maximizing these metrics. Interestingly, vapor condensation, as the final and most straightforward subprocess for freshwater production, has usually been neglected in performance evaluation. Each subprocess in the solar distillation exhibits unique features and functions, which plays critical role in the overall performance for freshwater production. In this section, performance evaluation methods for individual stage during the solar evaporation are provided, aims to clarify the corresponding underlying physical process and shed new insights on performance enhancement.

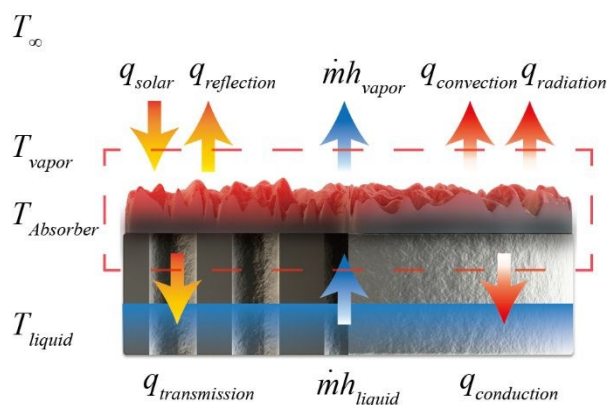


Figure 2 The three major processes governing the energy balance of the control volume (boxed in red dashes), including solar radiation, mass transport, and heat loss, indicated by arrows in orange, blue, and red, respectively.  $q$ , heat flux.  $\dot{m}$ , mass flow rate.  $h$ , enthalpy.

## 2.1 Solar-thermal Conversion

The solar-thermal conversion is the initial stage of solar-driven evaporation, which lays the foundation for freshwater generation. In general, solar-thermal conversion comprises two parts, light harvesting and photothermal conversion. The understanding of these process is of great importance to enhance the performance from the basic and motivate the development in exploring advanced system designs.

### 2.1.1 Light Harvesting

The light harvesting ability of the solar absorber is the prerequisite for attaining efficient light to heat conversion. When solar radiation is incident upon the surface of solar absorber, the irradiation may be reflected, transmitted, and absorbed. The absorption is the net energy inflow and can be expressed by

$$q_{\text{absorption}} = q_{\text{solar}} - q_{\text{reflection}} - q_{\text{transmission}} \quad 1$$

Absorptivity of the solar absorber  $\alpha$  is defined as the fraction of the solar radiation absorbed, reflectivity  $\rho$  as the fraction reflected, and transmissivity  $\tau$  as the fraction transmitted. Solar radiation possesses a spectrum which resembles a 5778 K blackbody, with deviations mainly due to atmospheric absorption and scattering, and majority of the irradiation energy lies in ultraviolet (~3%), visible light (~45%), and infrared band (~52%) with a wavelength range from 300 to 2500 nm<sup>37</sup>. As such, characterizations of materials' absorption, reflectivity, and transmissivity are conducted in this wavelength range. Since solar absorptance is a measure of the ability of a photothermal module to harvest solar energy. It is determined

by the ratio of the total acquired solar radiation to the incident radiation. Because most solar absorber appears opaque in this wavelength region, the transmissivity is commonly near zero. Therefore, the absorptivity  $\alpha$  can be experimentally determined by measuring the reflection at different wavelength and following

$$\alpha = \frac{\int_{300\text{nm}}^{2500\text{nm}} [1 - \rho_{\lambda}(\lambda)] G_{\lambda}(\lambda) d\lambda}{\int_{300\text{nm}}^{2500\text{nm}} G_{\lambda}(\lambda) d\lambda} \quad 2$$

where  $\rho_{\lambda}$  is the reflectivity and  $G_{\lambda}$  is the spectral irradiation, as a function of wavelength  $\lambda$ . Thus, the absorbed solar irradiation can be determined following

$$q_{\text{absorption}} = \alpha q_{\text{solar}} \quad 3$$

High absorptivity is a critical property of the solar absorber to achieve optimal efficiency. As discussed in following sections, owing to the innovations in topography and geometry design which significantly reduced the reflection, absorptivity has been able to reach over 95%.

### 2.1.2 Photothermal Conversion

Although light harvesting is a decisive ability to acquire solar energy, the subsequent photothermal conversion is crucial to generate heat to vaporize water. This process requires solar absorber to convert sunlight energy to thermal energy effectively, rather than radiative re-emission.

Various nanomaterials, including inorganic<sup>38, 39</sup> and organic materials,<sup>40, 41</sup> have been exploited for solar-driven evaporation. To compare the performance between different materials, the light-induced thermal generation is quantitatively analyzed with photothermal conversion efficiency. Conventionally, a direct experimental method to acquire photothermal conversion efficiency is by measuring the temperature variation under incoming light source. Typically, the solar absorber material is dispersed in solution phase and shined with a light source. The total mass, heat capacity, and light absorbance of sample material, as well as the light intensity, as other important factors are also taken into account to calculate the efficiency. With the same measurement of container system, the photothermal conversion efficiency of solar absorber material can be estimated. However, it is noteworthy that this method is typically for single wavelength light-to-heat conversion. For solar-driven evaporation, which occupy the whole spectrum of solar irradiation, it might be more reasonable to compare the thermal energy generation with the input solar energy within a defined period.



## 2.2 Water Evaporation

In order to maximize the vaporization efficiency, the generated heat should be occupied entirely for the purpose of water evaporation. However, in practice, heat dissipation will inevitably consume the thermal energy and undermine the evaporation efficiency. Thus, to control the thermal distribution during water evaporation, it is essential to take a look in the heat allocation. Herein, we summarize the critical factors that affect the heat occupation and describe the physical process with mathematical equation.

### 2.2.1 Heat Dissipation

As the temperature of the solar absorber and water within the control volume elevated above the surroundings, heat inevitably dissipates into the surrounding, resulting in energy loss. The heat transfer happens mainly by three routes, including conduction into bulk water, convection into the surrounding air, and radiation into the surroundings. The conduction heat flux  $q_{\text{conduction}}$  can be estimated by

$$q_{\text{conduction}} = \kappa \left. \frac{\partial T}{\partial x} \right|_{\text{border}} \quad 4$$

where  $\kappa$  is the conductivity of water and  $\left. \frac{\partial T}{\partial x} \right|_{\text{border}}$  is the temperature gradient at the border of the control volume, though estimating the temperature gradient is not a trivial task. The convection heat flux  $q_{\text{convection}}$  can be estimated by

$$q_{\text{convection}} = h(T_{\text{PTM}} - T_{\infty}) \quad 5$$

where  $h$  denotes the natural convection coefficient in a buoyancy-driven flow, which is mainly dependent on temperature and surface dimension.  $h$  can be estimated using empirical equations and is normally in the order of  $\sim 1 \text{ W m}^{-2} \text{ K}^{-1}$ .<sup>42-44</sup> The radiation heat flux can be calculated by

$$q_{\text{radiation}} = \varepsilon \sigma (T_{\text{PTM}}^4 - T_{\infty}^4) \quad 6$$

where  $\varepsilon$  is the emissivity of solar absorber surface,  $\sigma$  Stefan-Boltzmann constant, and  $T_{\infty}$  the temperature of surroundings.

Due to the empirical nature of heat flux calculation in general, the heat loss determined using these equations provides only a rough estimation. However, it offers important implications on strategies for the minimization of energy loss. For example, assuming the temperature of the solar absorber is  $41^{\circ}\text{C}$  and surrounds  $27^{\circ}\text{C}$ , the conductive, convective, and radiative heat

loss are  $\sim 2.3\%$ ,  $3.0\%$ , and  $\sim 4.0\%$  of the solar energy,<sup>43</sup> suggesting that the three heat loss mechanisms pose similar contribution.

### 2.2.2 Mass Flow of Water/Vapor

Liquid water flows into the control volume at a temperature of  $T_{\text{liquid}}$  and an enthalpy of  $h_{\text{liquid}}$ , evaporates at the surface of the solar absorber, and flows out of the control volume as vapor at a temperature of  $T_{\text{vapor}}$  with an enthalpy of  $h_{\text{vapor}}$ . The enthalpy change,  $\Delta h$ , can be estimated by adding sensible heat and phase change enthalpy, following

$$\Delta h = h_{\text{vapor}} - h_{\text{liquid}} = c_p (T_{\text{vapor}} - T_{\text{liquid}}) + h_{\text{lg}} \quad 7$$

where  $c_p$  is the specific heat and  $h_{\text{lg}}$  is the heat of evaporation at  $T_{\text{vapor}}$ , with the assumption that the dependence of  $c_p$  on temperature is negligible. However, we suggest that whenever applicable, the enthalpy change should be calculated using experimentally measured thermodynamic properties from thermodynamic databases.

The mass flow rate is usually determined by continuously monitoring the weight change of the water using an analytical balance. However, it should be noted that under dark condition, water also takes in heat from the surroundings and evaporates. As such, a proper control experiment should be performed, and the baseline mass flow rate generated under dark condition should be subtracted.<sup>10, 45</sup>

As we mentioned earlier in section 2.1.2, the photothermal conversion efficiency of solar absorber is difficult to be calculated according to the conventional method. However, from a systematic angle, such efficiency can be described as solar-to-steam conversion efficiency, which denotes the energy applied for water vaporization versus the total energy supply. Briefly, solar-thermal conversion efficiency  $\eta$  is described as the fraction of the solar irradiance that has been utilized to generate vapor. It can be calculated following

$$\eta = \frac{\dot{m} \Delta h}{q_{\text{solar}}} \quad 8$$

where  $\dot{m}$  is the mass flow rate.

Evaporation rate, which is essentially the mass flow rate  $\dot{m}$ , characterizes the productivity of the vapor generation process. As discussed in following sections, increasing the solar-thermal conversion efficiency and evaporation rate has been the goal of solar-thermal researches. Currently, researchers have been able to achieve a thermal efficiency up to  $94\%$ .<sup>46</sup> In the ideal case, water evaporates in an isothermal process with minimal

enthalpy change, and solar energy is completely converted to evaporation enthalpy of water. Under one sun illumination ( $1000 \text{ W m}^{-2}$ ) and assuming water temperature of  $25^\circ\text{C}$ , where  $\Delta h$  is roughly  $2400 \text{ kJ/kg}$ , the mass flow rate of the generated vapor is estimated to  $1.50 \text{ kg m}^{-2} \text{ h}^{-1}$ . This value can serve as a benchmark in the performance evaluation of the endeavours in system designs.

### 2.3 Vapor Condensation

Desalinated water can be collected by condensing the generated vapor. By reducing the temperature of the vapor below the saturation temperature  $T_{\text{sat}}$ , commonly known as the dew point, vapor condense into liquid water. In general, condensation can happen in three modes, including homogeneous condensation, where water droplets form within the vapor and result in a fog, direct contact condensation, where vapor contacts liquid water and merges into it, and surface condensation, where vapor touches a cold surface and condensate forms on the surface. Due to its ease in implementation, surface condensation is the most commonly adopted mode for water collection in solar stills.

Surface condensation can be initiated when vapor contact a surface with a temperature  $T_{\text{surface}}$  lower than  $T_{\text{sat}}$  and liquid nucleated on the surface. The condensation process is then driven by free convection of the vapor phase, and thus the geometry of the surface and the flow condition of the vapor phase have significant impact on the effectiveness of the condensation. Latent heat is released and transferred to the surface, and the total heat transfer can be calculated by<sup>42</sup>

$$Q_{\text{condensation}} = h_{\text{condensation}} A_{\text{surface}} (T_{\text{sat}} - T_{\text{surface}}) \quad 9$$

where  $h_{\text{condensation}}$  is the heat transfer coefficient due to condensation and  $A_{\text{surface}}$  is the area of the surface.  $h_{\text{condensation}}$  represents the effectiveness of the heat transfer in the condensation process and can be estimated using empirical equations. Once the value of  $h_{\text{condensation}}$  has been obtained, the mass flow rate of the condensate can be calculated by

$$\dot{m} = \frac{h_{\text{condensation}} A_{\text{surface}} (T_{\text{sat}} - T_{\text{surface}})}{\Delta h} \quad 10$$

where  $\Delta h$  is the enthalpy difference between saturated vapor and liquid water at  $T_{\text{surface}}$ . Therefore, to achieve optimal water production, the condensation heat transfer should be maximized. Equation 10 implies four major strategies to increase  $\dot{m}$ , including by reducing  $\Delta h$ , increasing  $h_{\text{condensation}}$ ,  $A_{\text{surface}}$ , and the difference between  $T_{\text{sat}}$  and  $T_{\text{surface}}$ .

Upon condensation on the surface, the condensate can form either a liquid film or drops, in processes termed film condensation or dropwise condensation, respectively, depending on the surface properties. In general, hydrophilic surfaces, such as glass surfaces, lead to film condensation, and hydrophobic surfaces, such as plastic surfaces, lead to dropwise condensation. In either case, the condensate poses additional thermal resistance and thus hinders the heat transfer. In dropwise condensation, condensate occupies less surface area, and the  $h_{\text{condensation}}$  can be significantly larger than that in film condensation.<sup>42</sup> However, solar irradiation normally needs to pass through the condensation surface before reaching the photothermal materials in most solar stills, and drops generate significant reflection, drastically reducing the efficiency of solar absorption.<sup>21</sup> Therefore, it was recommended that hydrophilic surfaces should be used for condensation in solar still. The inclination of the surface can affect the retrieval of the condensate and its accumulation on the surface, thus also affecting the  $h_{\text{condensation}}$ . As such, researchers have looked into the effect of inclination angle on vapor condensation.<sup>21</sup> In addition, active removal of the condensate from the surface by wiping or vibration was also reported as an attempt to enhance the heat transfer.<sup>47</sup>

The efficacy of increasing  $A_{\text{surface}}$  is straightforward and has indeed been confirmed in the effort of maximizing the condensate production.<sup>22</sup> Several methods have also been proposed to increase the difference between  $T_{\text{sat}}$  and  $T_{\text{surface}}$ . Essentially, any methods that increase solar absorption and water evaporation can boost the humidity within the chamber, which in turn increases  $T_{\text{sat}}$ . Since vapor condensation releases latent heat on the surface, heat must be effectively dissipated from the surface to surroundings to prevent  $T_{\text{surface}}$  from rising. To achieve this goal, measures such as cooling the surface and using thinner surface to accelerate heat conduction have been tested.<sup>48, 49</sup>

### 3. System Designs for Energy Manipulation

Sunlight capture and photothermal generation are of the great importance in solar-driven evaporation. In the past few years, numerous research works have been devoted to developing photothermal materials with broadband sunlight absorbance<sup>32, 50</sup> and promising heat conversion efficiency.<sup>51</sup> Various types of novel materials, including plasmonic nanoparticles,<sup>52-55</sup> carbon-based materials,<sup>56-62</sup> MXene membranes,<sup>38, 63, 64</sup> and semiconductor nanomaterials,<sup>65-67</sup> have been studied and reformed to achieve efficient sunlight capture and thermal generation. Readers who are interested in the details of photothermal generation, material selection, and material design, can find more information in the reviews by Gao et al.<sup>31</sup> Currently the performance of photothermal conversion is approaching to the ceiling. In order to further pursue the water evaporation rate in solar evaporation system, the research

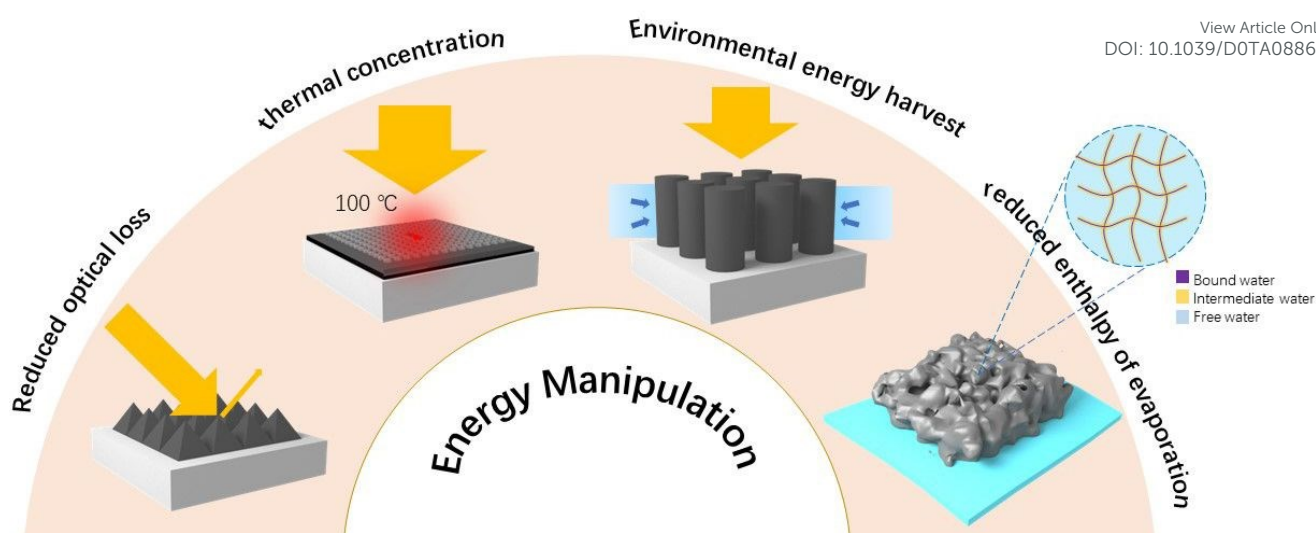


Figure 3 The schematic demonstration of energy manipulation strategies.

focus is gradually shifted to the system designs with sophisticated energy management from materials investigation.<sup>68-71</sup> Under the assumption of excellent heat conversion efficiency, several strategies are proposed that can be employed for the judicious design of solar evaporation systems endowed with superior energy utilization, including 1) strengthened the sunlight captures with modified surface topography; 2) increased thermal accumulation by concentration scheme; 3) recovered additional energy from the environment, and 4) reduced the enthalpy change of evaporation, as shown in Figure 3. The following sections will discuss the proposed strategies in detail to demonstrate the relationship of system designs and energy manipulations.

### 3.1 Modification of Surface Topography

In the past few years, great progress has been made to develop interfacial solar evaporators with promising light absorption (covering the entire solar spectrum)<sup>72</sup> and remarkable photothermal efficiency.<sup>33</sup> Although higher energy utilization efficiency has been realized, compared to the volumetric system, the membrane based interfacial solar evaporators still suffered from significant optical and energy losses,<sup>14, 73, 74</sup> regardless of the light absorbing properties of the photothermal materials. Such losses are originated from the diffuse reflectance and thermal radiation, which compromise the energy influx and water evaporation. Moreover, in practical condition, the changes of solar angle might be another issue to affect the solar absorbing and vapor production.<sup>12</sup> Hence, to address the aforementioned challenges, solar evaporators with designed surface topography is emerging in recent years.

#### 3.1.1 Enhance light absorption by multiple reflections

One of early works which aimed to recover the dissipated light energy and thermal energy was proposed by Shi and co-workers, who created a cup-shaped solar absorber to reduce energy loss.<sup>16</sup> The reflected energy from the evaporator basin can be efficiently re-absorbed by multiple reflections, providing extra energy for heat generation. Specifically, a maximum evaporation rate of  $2.04 \text{ kg m}^{-2} \text{ h}^{-1}$  was achieved under one sun irradiation with optimal cup structure, and such value was far higher than that of the 2D planar system ( $1.21 \text{ kg m}^{-2} \text{ h}^{-1}$ ). A similar strategy which aims to recover the reflected sunlight was introduced by Xu et al., who designed an origami solar absorber made of pencil-drawn paper.<sup>75</sup> Compared to the planar system, the origami system with a folded angle of  $90^\circ$  has 41% larger surface area, which is beneficial for solar absorption and water evaporation. In the field experiment, the distillate productivity of the origami system was 22% higher than the planar system, owing to the re-absorption of dissipated sunlight. Wang and co-workers fabricated an artificial 3D cone composed by polypyrrole (PPy)-coated polyvinylidene fluoride (PVDF) membrane to study the structure-energy nexus.<sup>76</sup> As shown in Figure 4a, a series of samples with tunable apex angles ( $180^\circ$ ,  $121^\circ$ ,  $86^\circ$ ,  $70^\circ$ , and  $56^\circ$ ) are prepared to investigate the effect of the opening angles on photothermal performance. Owing to the structure-dependent optical properties, the surface temperature increased as the apex angle becomes smaller. A maximized solar evaporation rate of  $1.70 \text{ kg m}^{-2} \text{ h}^{-1}$  was achieved with optimized cone apex angle, which was nearly 1.7 times higher than that of the corresponding planar system.

The complexity of the surface structure of solar absorbers was proved to be effective to influence multiple reflections. Another



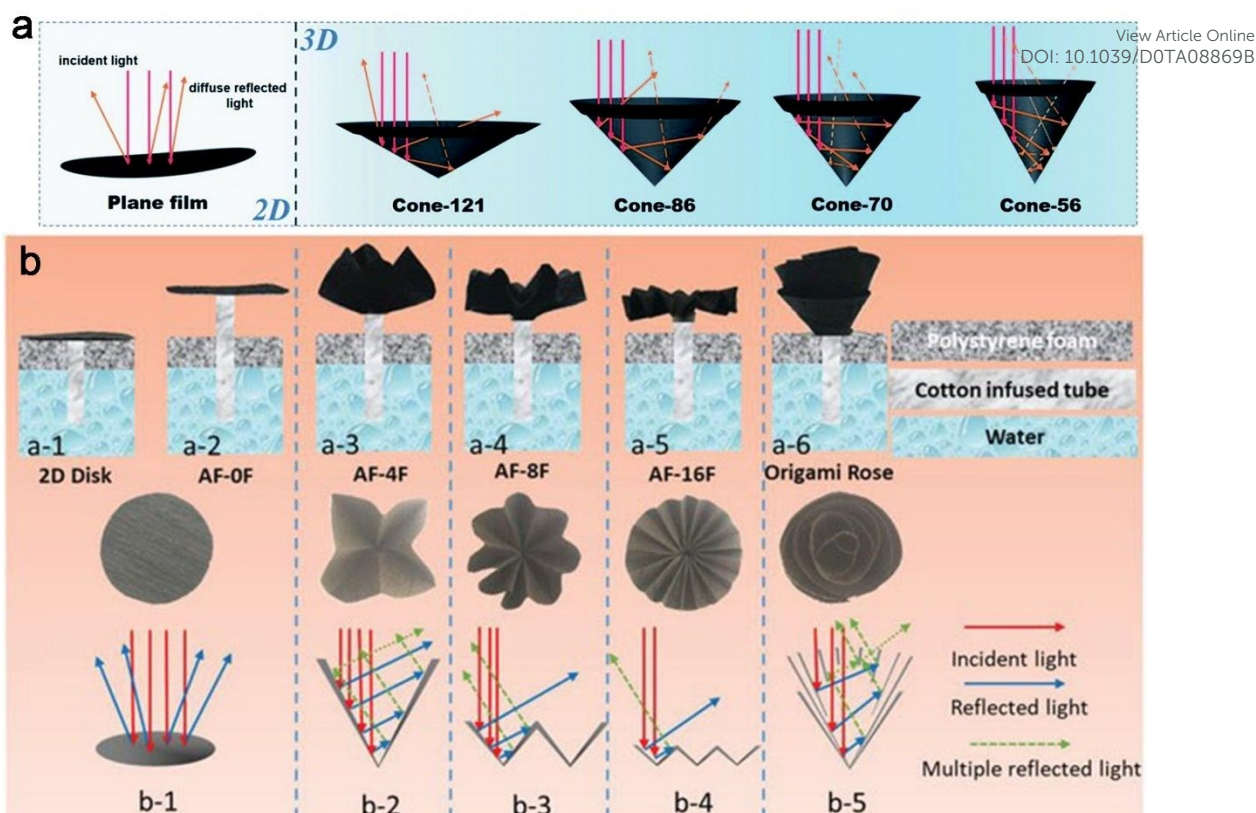


Figure 4 Schematic of the energy recovery by solar evaporation system with designed surface topography. a) Artificial 3D cone-shaped structure. Reproduced with permission.<sup>70</sup> Copyright 2018, Royal Society of Chemistry. An isolation PPy-based origami solar evaporation system with flower-like surface topography. b) The schematic of the structure of solar evaporation systems and the light-matter interaction. Reproduced with permission.<sup>71</sup> Copyright 2018, Wiley-VCH.

origami-type solar evaporator with flower-like surface topography was designed by Li and co-workers.<sup>77</sup> According to Figure 4b, origami structures with individual folding structures (AF-0F, 4F, 8F, 16F, and Origami Rose) are prepared to demonstrate the light-matter interaction. It has been found that the number of petals and the depth of the folded area are both critical to the overall light absorption and water evaporation rate. Hence, the Origami Rose Sample, with the most petals and deepest depth can afford the most rounds of light reflections, exhibited the highest optical absorption of 99% and water evaporation rate of  $2.12 \text{ kg m}^{-2} \text{ h}^{-1}$  under one sun irradiation. However, it is worth to mention that even though the Origami Rose possessed the best energy utilization in this work, the surface temperature was much lower than the planar PPy disk during the solar evaporation experiments. Such finding may contradict to the previous concept that higher surface temperature can induce stronger water evaporation. According to the authors, the enlarged surface area of the Origami Rose can afford extensive evaporation, hence gave rise to lower thermal accumulation than that in planar device. Furthermore, low surface temperature was also beneficial for reducing the radiative energy loss and improve the energy utilization efficiency.

By modifying the surface topography of solar absorber, the performance of solar evaporation is hugely improved due to the enhanced sunlight capture, stronger heat generation, and enlarged evaporation area. Currently, the design of surface structures of solar absorbers plays a more significant role in performance enhancement than materials investigation. However, there are still many issues still need to be solved. For example, although more dissipated energy can be reabsorbed with the heightening sidewall and consequently generated higher temperature, the solar absorber may afford higher inner humidity and hence inhibit vapor production. In this case, the sustainability of solar-driven evaporation device may be greatly hindered. Hence, there is still much room for further modification.

### 3.1.2 The evaporation of solar absorber with matrix form

It is clear that the surface topography is crucial for efficient solar energy utilization. The previous examples demonstrate the effect of multiple reflections and evaporation areas on the overall performance of vapor production on a single unit. In a more practical situation, a matrix of evaporation unit is required to against large scale freshwater generation.



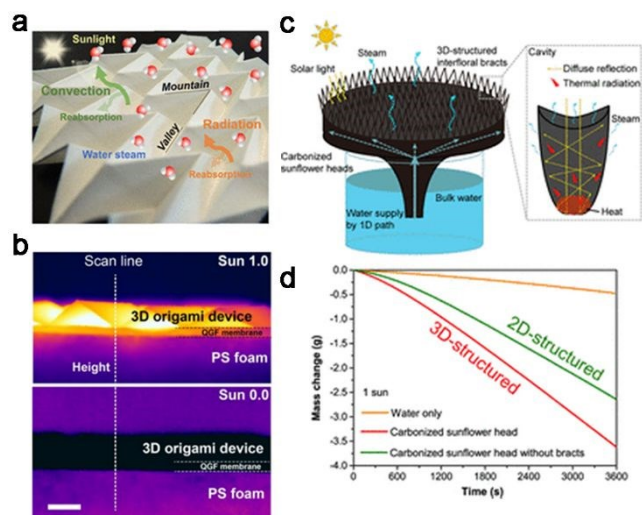


Figure 5 a) The solar evaporation system with surface structure of periodic pleats. b) The temperature distribution of 3D origami device with/without 1 sun irradiation. Reproduced with permission. <sup>72</sup> Copyright 2018, American Chemical Society. c) The solar evaporation system made of carbonized sunflower head. d) The water evaporating performance of carbonized sunflower head. Reproduced with permission. <sup>73</sup> Copyright 2020, American Chemical Society.

Hong and co-workers reported an origami-type solar evaporation system with surface structure of periodic pleats.<sup>78</sup> As indicated in Figure 5a, the periodic surface structure contains repeated unit with valley and peak, which composed of four parallelogram faces. With increasing surface areal density (Aactive/Aproject: the ratio of the evaporation area to the projection area), the vapor production was increased due to the enhanced light capture and heat loss recovery. With the optimal areal density of 4.65, nearly 100% of solar energy efficiency was absorbed with an evaporation rate of  $1.59 \text{ kg m}^{-2} \text{ h}^{-1}$ , which was nearly 50% higher than that of planar system. To obtain more insight on the energy utilization phenomenon, infrared camera was used to capture the temperature distribution in the origami system during the evaporation experiments. An inhomogeneous spatial temperature distribution was observed across the proposed origami periodic surface. As shown in Figure 5b, with and without the sunlight illumination, the valley folds always exhibit higher temperature than the mountain folds in wet state. Such phenomenon can be explained by the stronger water evaporation on the mountain fold. In addition, due to the temperature gradient on each unit cell, thermal energy can be further re-utilized due to the heat flux from the bottom to the top. Thus, both the reduced light reflection by the concave structure and the inverse heat flux resulted in the promising energy utilization. A similar isolation solar evaporation device made of PPY-functionalized cellulose paper with tunable microstructures and macroscopic geometries was proposed by Ni and his co-workers.<sup>15</sup> By folding the PPY-paper into 3D “cootie-catcher-shaped” structure, a water evaporation rate of  $2.99 \text{ kg m}^{-2} \text{ h}^{-1}$  was achieved under 1 sun irradiation, far succeeding the value ( $1.47 \text{ kg m}^{-2} \text{ h}^{-1}$ ) of 2D device.

The periodic undulating surface structure can also be seen in the nature. Sun et al. used carbonized sunflower heads to achieve efficient solar vapor generation.<sup>79</sup> As shown in Figure 5c, owing to the numerous 3D cavities on the top surface, solar energy can be absorbed extensively with minimized energy diffuse reflectance and thermal radiation. In addition, the hugely enlarged evaporation area was beneficial for water evaporation. Due to the structure feature, a solar evaporation rate of  $1.51 \text{ kg m}^{-2} \text{ h}^{-1}$  and an evaporation efficiency of 100.4% was achieved under one sun illumination (Figure 5d). In contrast, for carbonized sunflower head without the top bracts gave a much-reduced solar evaporation rate of  $1.18 \text{ kg m}^{-2} \text{ h}^{-1}$  and evaporation efficiency of 78.4%.

In practical applications of solar evaporation, it is very important to consider the matrix form of solar absorber. It is believed that the density and shape of the solar absorber unit may hugely affect the light absorption and vapor generation. However, as far as we concerned, there is no research study to investigate and compare the overall performance of solar-driven evaporation systems in unit and matrix form. We may still acquire some insights from the research works mentioned above. For example, Hong’s work indicated the relationship between surface areal density and vapor generation rate, which may provide a rough direction for future development of solar evaporation system with matrix form.

### 3.1.3 Compensation for the incident angle effect

Although great progress has been made to achieve smart energy management and efficient water evaporation at labs, perform solar vapor generation in outdoor environment is quite different and more parameters need to be considered. One of the most significant issues in the practical experiment is the unstable sunlight intensity. In laboratory experiment, solar vapor devices are always shined by simulated sunlight perpendicularly with the stable intensity of  $1 \text{ kW m}^{-2}$ . However, in practical outdoor condition, the sun moves through the sky with changed elevation angles throughout the day. In most cases, only 50-90% of sunlight could arrive at the solar receiver surface, depends on the weather conditions (nearly 10~20% of energy diffusion occurs on sunny days and 50% occurs on cloudy days).<sup>12</sup> Moreover, the randomly moved clouds would occasionally block the sunlight. In this case, there is a little chance for solar evaporation system to operate with full potential.

An umbrella-shaped evaporation device made of graphene oxide film was designed by Li et al.<sup>80</sup> As shown in Figure 6a, due to the promising light absorption of the graphene oxide and the umbrella-shaped morphology, the proposed 3D device can acquire sunlight from different incident angles. In the field experiment, nearly 24% enhancement of sunlight absorption was realized by the umbrella-shaped device, resulted in 1.43 times higher of vapor generation than planar device. A similar

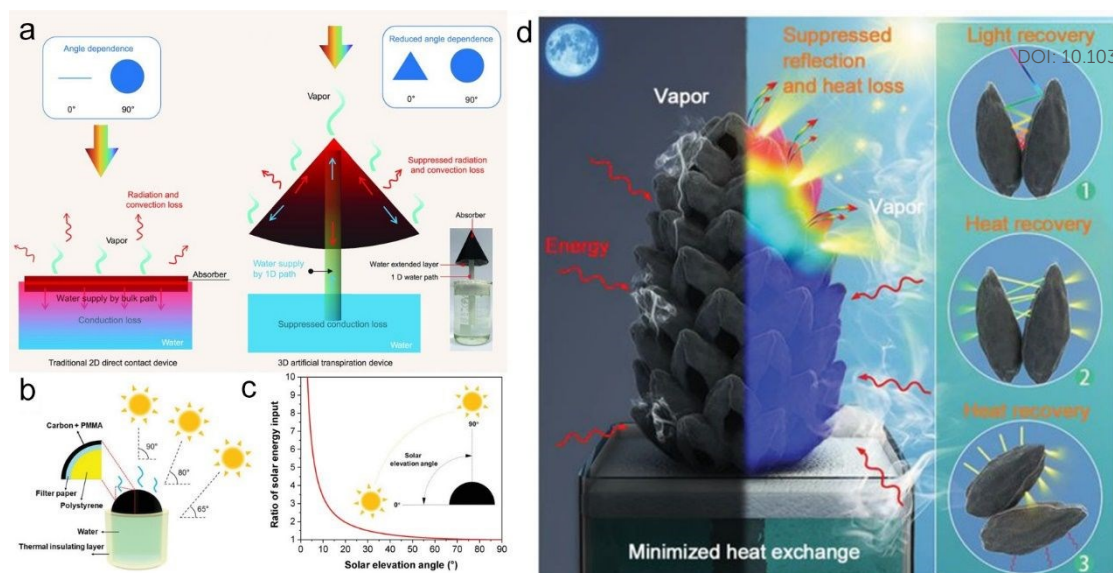


Figure 6 Several isolation solar evaporation systems with designed surface topography for offsetting the angle of the incidence effect. a) The umbrella-shaped system. Reproduced with permission.<sup>74</sup> Copyright 2017, Oxford University Press. b) The hemispheric-shaped system and c) its performance cope with varied light incident angles. Reproduced with permission.<sup>12</sup> Copyright 2020, American Chemical Society. d) The carbonized tree-like furry magnolia fruit. Reproduced with permission.<sup>75</sup> Copyright 2019, Wiley-VCH.

work has been reported by Chen and co-workers.<sup>12</sup> In order to compensate the varied solar elevation angles, a 3D hemispheric solar-driven evaporation device was designed. As shown in Figure 6b and 6c, high ratio of solar energy input is achieved by the 3D hemispheric device with varying solar elevation angle from 0 to 90 degrees. In order to simulate the outdoor conditions, 2D planar, cylindric, and 3D hemispheric devices were irradiated with wide incident angles (90°, 80°, and 65°) under moderate intensity (0.75 sun). The experimental results demonstrated that the water evaporation rate and energy efficiency of 3D hemispheric device remained constant while the performance of the other two systems downgrades drastically with decreasing incident angle. The hemispheric surface was capable to maintain the highest solar energy input from 0° to 90°, which possessed promising potential to prolong the working period throughout the day. Moreover, hemispheric structure exhibits the best performance in coping with the variation of solar angles in both indoor and outdoor experiments. After 3 hours of sunlight illumination in the field experiments, a solar evaporation rate of 4.83 kg m<sup>-2</sup> was obtained by the 3D hemispheric system, which was 15.8% higher than cylindric system (4.17 kg m<sup>-2</sup>) and 50.5% higher than 2D planar system (3.21 kg m<sup>-2</sup>).

The nature ready provides an elegant solution for efficient solar vapor generation. In recent years, the carbonized biomasses have received especial attention in solar vapor generation, due to its intrinsic surface structure for light trapping, fast water evaporation, thermal loss reducing, efficient water transportation, and good scalability. Bian and co-workers

introduced a highly efficient solar evaporation system made of carbonized tree-like furry magnolia fruit.<sup>81</sup> As indicated in Figure 6d, owing to the unique surface structure, which composed of numbers of carpel, multiple sunlight reflection was occurred, which efficiently recover and recycle the incident solar energy, resulted in ~98.5% of solar utilization efficiency. In addition, the large surface area and additional available free space (offered by the staggered pod-like carpels) afforded fast vapor escape with reduced vaporization enthalpy, which boosted the vapor production throughout the day. Hence, an impressive solar vapor generation rate of 1.22 kg m<sup>-2</sup> h<sup>-1</sup> in dark and 3.15 kg m<sup>-2</sup> h<sup>-1</sup> under 1 sun irradiation was achieved. Similar to the 3D hemispheric system mentioned previously, the tree-like isolation solar evaporation system can also collect more sunlight throughout the day than 2D planar system. In the outdoor experiment (from 7:00 a.m. to 6:00 p.m.), a remarkable vapor production rate of 15.6 kg m<sup>-2</sup> was obtained by the tree-like system, far succeeding that (4.2 kg m<sup>-2</sup>) of the 2D evaporator with the same ground area.

Previous mentioned designs compensated the variation of solar angles by always making sure that the surface of solar absorbers can be shined by sun. However, it is impossible to absorb the solar energy maximumly throughout the day. In contrast to compensate the solar absorption loss passively with pre-designed surface structures, Qian et al.<sup>82</sup> developed an artificial phototropism (sunflower-life biomimetic omnidirectional tracker, SunBOT) for omnidirectional light harvesting. The proposed SunBOT system is composed of nanostructured thermal stimuli-responsive polymers and photothermal nano-

agents. Similar to the biological asymmetric growth of plants under light exposure, the SunBOT is able to bend towards light source due to the asymmetric deformation between the shined high-temperature region and the un-exposure low-temperature region. The tropistic locomotion of SunBOT is further applied in solar evaporation system. An array of SunBOTs can accurately response and turn to the light source. In this case, the incidence energy loss is hugely recovered with up to 400% enhancement of solar evaporation in an operation window of  $164^{\circ}$  ( $-82$  to  $82^{\circ}$ ), compared to non-tropistic surface.

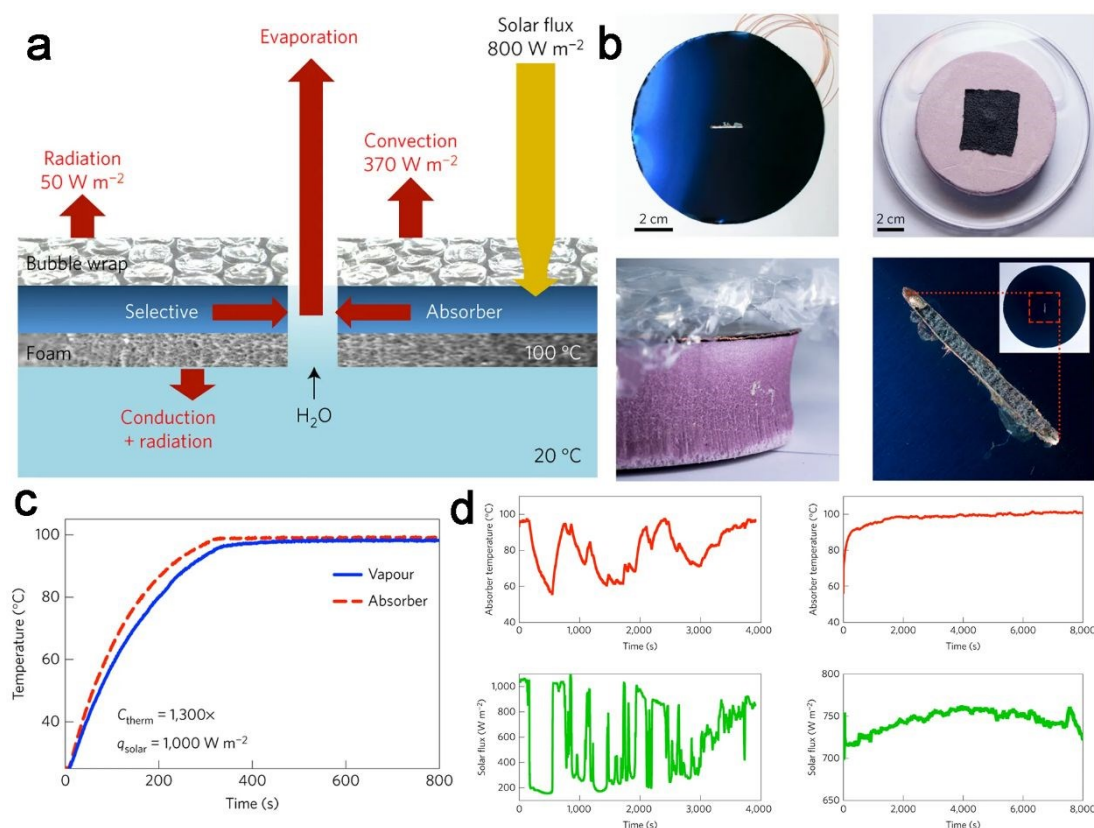
It is of great significance to against the variation of solar angles in practical applications. The early trials mostly rely on the structure features of solar absorbers, however, inevitably left some surface in shallow, which undermine the full potential of solar-driven evaporation. Recently, solar absorbers with the ability to chase and face to the light source are reported. Such designs may significantly improve the solar evaporation performance by achieving maximum sunlight absorption throughout the day. However, such designs are still in the infant stage, for which the proposed structure may be too fragile to be applied in practical situation. Hence, further improvement of the structure designs of solar absorber is required to achieve higher energy manipulation efficiency.

### 3.2 Energy Concentration Scheme

View Article Online  
DOI: 10.1039/D0TA08869B

Solar-thermal technology, which converts solar energy into thermal energy, has been extensively constructed for industrial activities few decades ago. In the typical design of solar-thermal plant, solar concentrator, solar energy receiver and heat-transfer fluid were included. With the solar tracking and concentrating functions, the power of light energy can be intensified as high as 1000 folds with the operating temperature over  $400^{\circ}\text{C}$ .<sup>83</sup> Although the conventional-thermal technology was only occupied in industrial electricity generation, the heating mechanism could also provide new impact on solar vapor generation.

In the field of solar vapor generation, with enhanced power density of simulated solar light, hugely improved water evaporation rate has been achieved by interfacial systems. Zhu and co-workers combined plasmonic nanoparticles with carbonized wood<sup>62</sup> to achieve highly efficient solar vapor generation under concentrated incident light. Specifically, under 10 suns of illumination,  $11.8\text{ kg m}^{-2}\text{ h}^{-1}$  of water evaporation rate was accomplished, far beyond the reported value under one sun. Mu and co-workers fabricated carbon aerogel 11 consist of hollow carbon nanotube to achieve an evaporation rate of  $\sim 4.2\text{ kg m}^{-2}\text{ h}^{-1}$  under 3 suns with surface temperature of  $54.6^{\circ}\text{C}$ . Such values were much higher than





that ( $\sim 1.44 \text{ kg m}^{-2} \text{ h}^{-1}$  of water evaporation rate and  $40.5^\circ\text{C}$  of surface temperature) under 1 sun. Yang and co-workers prepared a photothermal membranes composed of single wall carbon nanotubes and  $\text{MoS}_2$  films.<sup>39</sup> The proposed membrane exhibited  $6.6 \text{ kg m}^{-2} \text{ h}^{-1}$  of water evaporation rate and  $106^\circ\text{C}$  of surface temperature, under 5 suns of irradiation.

Without a doubt, the overall water evaporation rate is positively correlate with the total energy received by the system. With more solar energy absorbed, more thermal energy generated, resulted in dramatically enhanced water evaporation rate. However, in practical conditions, integrating an optical concentrating component ( $\text{US\$200m}^{-2}$ ) will hugely burden the fabrication and maintenance costs. Hence, an energy concentration scheme with facile preparation process is highly desired for efficient solar evaporation.

In order to address this challenge, Ni and co-workers provided a novel strategy which can thermalize a floating solar receiver to  $100^\circ\text{C}$  in ambient environment without light concentrator.<sup>44</sup> The typical structure of the solar evaporator is shown in Figure 7a, which the photothermal material is surrounded by heat insulation layers with a middle-drilled channel. In this case, the generated heat can be localized in the confined area and concentrated for water vaporization. The specific material compositions and device structure are indicated in Figure 7b. Although the top bubble wrap layer partially ( $\sim 20\%$ ) reduced the solar influx, the convective heat loss driven by the solar-thermal process was also hugely diminished. As shown in Figure 7c, under one sun illumination, the maximum vapor temperature of  $98^\circ\text{C}$  is achieved with the thermal concentration  $C_{\text{therm}}$  (the ratio of the illumination area to the evaporation area) of 1,300x. Such high temperature was contributed to the heat localization and thermal concentration strategy. The practical performance of this solar vapor system was evaluated in outdoor environment. As shown in Figure 7d, remarkably, even with varying solar flux ( $\sim 200\text{--}1,000 \text{ W m}^{-2}$ ) and wind speed, the solar vapor system was able to recover its peak operating temperature ( $>95^\circ\text{C}$ ) within minutes. Moreover, according to the simulation results, big tolerance on the properties of top covering and solar influx were found, making the proposed solar vapor system operable in diverse weather conditions. Generally, the strategy proposed herein significantly reduces the energy losses and accumulate thermal energy for intensified vaporization, providing a new insight on solar energy utilization. Similar structure design with energy concentration capability at the evaporation front has been fabricated by Guo and co-workers.<sup>25</sup> The solar evaporation device was composed of a PVA hydrogel top layer and activated carbon paper as the photothermal bottom layer. With the tailored surface topography on PVA layer, increased solar energy was harvested and consequently generated higher temperature for water evaporation. Strikingly, a water evaporation rate of  $\sim 2.6 \text{ kg m}^{-2}$

$\text{h}^{-1}$  and solar energy efficiency of  $\sim 91\%$  were achieved only under one sun irradiation.

DOI: 10.1039/D0TA08869B

### 3.3 Energy Recovery from the Surrounding

In the previous sections, efforts devoted to enhancing the water evaporation rate by improving the solar light absorption and applying thermal management has been discussed. Those methods required an elaborated surface topography<sup>81</sup> or enlarged evaporation area<sup>84</sup> to accelerate water-vapor phase transition. Although considerable progress has been made to minimize the heat loss from the photothermal components in the past few years, the theoretical limit of water evaporation rate (based on the fixed solar energy input per unit area) is the huge roadblock impedes the further development.<sup>34</sup>

In order to overcome the natural limitation, Song and co-workers discovered a new mechanism to boost water evaporation by generating cold vapor below room temperature.<sup>85</sup> Unlike the thermal confinement strategy mentioned previously, the authors actively ameliorated the effect of heat insulator in order to enhance the heat exchange of solar evaporator with ambient environment. Under low-density solar illumination (0.2 sun), low surface temperature (below room temperature) and high evaporation rate (higher than the theoretical limit under the same solar input) were achieved. According to the authors, the increment of water evaporation was originated from the additional energy absorption from the warmer environment. When the temperature of evaporator was higher than the ambient with high-density solar flux (0.6 sun), environmental energy was no longer available for the evaporator, hence cannot be absorbed to promote the water evaporation rate. In order to implement this strategy under 1 sun irradiation, solar evaporators with enlarged surface areas and apex angles were prepared. As indicated in Figure 8a, with the optimal apex angle of  $\sim 22.4^\circ$ , an evaporation rate of  $2.20 \text{ kg m}^{-2} \text{ h}^{-1}$  was accomplished under the 1 sun illumination. Certainly, absorbing energy from the warmer environment provided a novel solution to beyond the theoretical limits of solar-driven water evaporation.

A similar finding was reported by Li and co-workers,<sup>86</sup> who fabricated a smart solar evaporator, which could absorb solar energy and gain environmental energy simultaneously. The solar evaporation system was composed of an array of cylindric column, which constructed by a cotton core and carbon nanoparticles decorated cellulose warps. As shown in Figure 8b-c, under simulated sunlight irradiation, the top surface can efficiently absorb solar energy and generate heat, in the meanwhile, the side surface with low temperature can absorb energy from the environment. Hence, highly enhanced water evaporation rate was achieved by this system, which far succeeding the corresponding theoretical limits at varied light intensities.



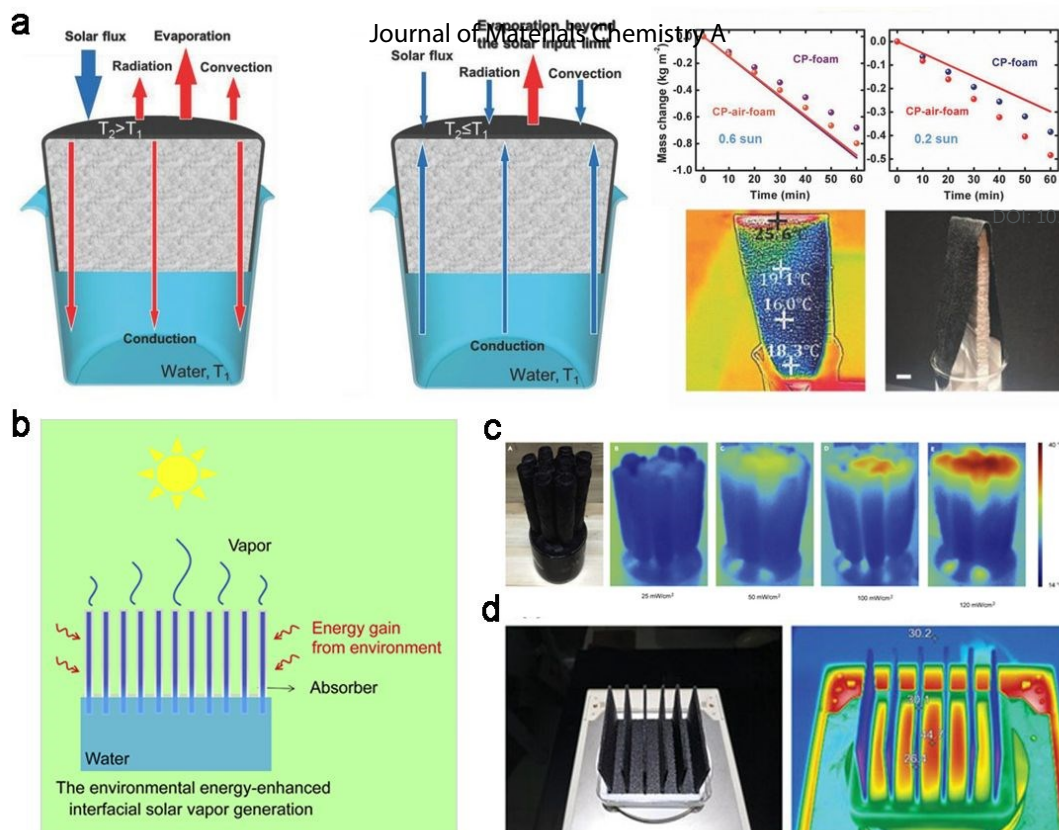


Figure 8 Environment energy-harvesting evaporators. a) Energy flow of the carbon paper on polystyrene foam under strong light illumination and low light illumination or in darkness; the performance of the prepared solar evaporator device with unique configuration under different solar intensities are demonstrated. Reproduced under the terms and conditions of the CC BY 4.0 License. <sup>79</sup> Copyright 2018, Wiley-VCH. b) The energy flow of solar evaporation system composed of an array of cylindrical columns. c) The temperature distribution of cylindrical evaporation system under different light intensities. Reproduced with permission. <sup>80</sup> Copyright 2018, Elsevier. d) The configuration and temperature distribution of the plug-in-type black nylon fiber (BNF) flocking boards system. Reproduced with permission. <sup>81</sup> Copyright 2019, Wiley-VCH.

Tu et al. <sup>87</sup> prepared a plug-in-type black nylon fiber (BNF) flocking boards system with an evaporation rate of  $2.09 \text{ kg m}^{-2} \text{ h}^{-1}$  under 1 sun irradiation. With the combination effects of photothermal phenomenon and cold vapor generation, the water evaporation performance was well beyond the corresponding upper limit of  $1.50 \text{ kg m}^{-2} \text{ h}^{-1}$ . The previously mentioned research work reported by Bian et al. <sup>81</sup> also utilized the strategy, which gaining the energy from the environment. As shown in Figure 8d, the carbonized magnolia fruit always had lower side surface (bottom part) temperature than the surrounding environment under solar irradiation. Such condition was attributed to the strong natural vapor production, which was also beneficial for gaining energy from the warmer environment. Hence, an extremely high evaporation rate of  $3.15 \text{ kg m}^{-2} \text{ h}^{-1}$  under 1 sun illumination was obtained in their work.

Although the integration of environmental energy absorption efficiently increased the system input for vapor production and generated water evaporation rate far beyond the theoretical limits, a new scientific question on cold vapor condensation for freshwater collection was introduced. It is challenging to release the thermal energy from the cold vapor, which the temperature below room temperature, with conventional condensation method. Thus, to optimize the freshwater generation with gaining environmental energy, there is a long way to go.

### 3.4 reduced the enthalpy of evaporation

As mentioned in above sections, much effort has been devoted to improving the solar evaporation rate through enhancing sunlight absorbance and energy manipulation by architecture designs. Actually, the vapour production rate ( $\dot{m}$ ) is determined by  $\dot{m} = \eta * q_{\text{solar}} / \Delta h$ , where  $\eta * q_{\text{solar}}$  is the absorbed solar energy and  $\Delta h$  corresponds to the specific enthalpy change of liquid water to vapor. Apart from increasing the energy input for water evaporation, it has been found that the regulation of enthalpy is a powerful strategy to strengthen vapor production. The enthalpy of vaporization is the amount of energy required to induce the phase transition from liquid water to vapour. With constant enthalpy of water evaporation ( $2444 \text{ J g}^{-1}$ ) and 1 sun irradiation, operating at the theoretical best, a conventional planar solar evaporator can only generate vapour at  $1.47 \text{ kg m}^{-2} \text{ h}^{-1}$ . Hence, the reduction of enthalpy is considered as a promising way to overstep the theoretical upper limit of water evaporation.

Recent advances in materials science reported methods to adjust the enthalpy of water evaporation. The water state in hydrogel network has been manipulated to affect water evaporation. Due to the water-solubilizing groups in polymer chains, such as hydroxyl groups, amino groups, carboxylic groups, and sulfonic acid groups, water molecules can bond with polymers with noncovalent interaction such as hydrogen

bonding and electrostatic interaction.<sup>88</sup> As reported by Yu's group,<sup>23</sup> three types of water state, including bound water, intermediate water, and free water, have been found in water-filled polymeric structure. Among them, intermediate water, which exists between free and bound water, requires the least energy to be activated for evaporation. Hence, photothermal hydrogel with higher degrade of crosslinking exhibited strong solar evaporation effect. Specifically, with the optimal inner structure, PVA hydrogel (loaded with PPy) required less energy demand for water evaporation, which is which is  $\sim 1400 \text{ J g}^{-1}$ . Accordingly, a record high evaporation rate of  $3.2 \text{ kg m}^{-2} \text{ h}^{-1}$  was achieved. In addition, the enthalpy can be further tailored by architecting polymer networks. According to Zhou et al.,<sup>89</sup> the introduction of chitosan can further reduce the energy demand of water evaporation, due to the co-existence of amine groups and increased amount of intermediate water. Hence, a water evaporation rate of  $3.6 \text{ kg m}^{-2} \text{ h}^{-1}$  was achieved by chitosan/PVA hydrogel (loaded with Ppy). Inspired by the reduced enthalpy of Chitosan/PVA hydrogel, Guan and his co-workers applied bacterial cellulose (BC) to achieve high proportion of intermediate water. Due to the ultrafine 3D cellulose network of BC, 69% of intermediate water was observed in BC hydrogels, resulted in a highly reduced enthalpy of  $997 \text{ J g}^{-1}$ . Attributed to reduced enthalpy and energy management designs, water evaporation rate of  $2.9 \text{ kg m}^{-2} \text{ h}^{-1}$  was achieved.

The reduced phase transition enthalpy was also been found in surface-burnt wood sample. According to Tang et al.,<sup>90</sup> by regulating the hydrophilicity of a surface-burnt wood and adjusting the height of the wood above a water surface, the enthalpy of water evaporation in wood can be reduced from 2444 to  $1769 \text{ J g}^{-1}$ . Such enthalpy change was mainly attributed to the state transition of water from "gravity state" to "capillary state". In such case, the microchannels of wood were not blocked by water but dredged with transpiration and resulted in much more evaporation spaces. In addition, during water evaporation, vapour was formed in single molecules or clusters which consisting of a few to tens of molecules. Less energy was required for water clusters to escape from bulk water than single molecules. Hence, due to the reduced enthalpy of  $1769 \text{ J g}^{-1}$ , a high evaporation rate of  $1.93 \text{ kg m}^{-2} \text{ h}^{-1}$  under one sun irradiation was achieved by the wood-based evaporator.

In real-world scenario, diffuse natural sunlight may not meet the energy requirement for efficient water evaporation. Hence, developing new materials with lower energy demand for water evaporation is a promising approach to achieve rapid solar distillation under natural sunlight is anticipated. Reduced the enthalpy of evaporation, has no doubt, sheds new light on such goal.

#### 4. System Designs for Water Transportation

View Article Online

DOI: 10.1039/D0TA08869B

Regardless of the progress achieved in optical and thermal energy management, the liquid transportation<sup>91</sup> is another important issue to affect the overall solar evaporation performance. Although the radiant heat can be reduced through surface structural designs and temperature control, as mentioned in the last section, water transportation from bulk water to the evaporation surface, taking most of thermal energy, is considered as the major heat draining pathway. Hence, reduced the water convection loss is of great importance to achieve high energy efficiency and water evaporation rate.<sup>92,93</sup> Furthermore, in the continuous and long-term operation, a fact that cannot be ignored is that the escape of a large amount of water vapor may accompany with the accumulation of salt crystals in the evaporation system.<sup>62,94</sup> The solid crystals not only clogged the water and vapor transportation pathways<sup>95-97</sup> but also reflected the sunlight<sup>98</sup> and reduced the solar input, resulted in deteriorated freshwater productivity. Recent progress in solar water evaporation explored various liquid manipulation schemes, which was feasible to limit the heat convection loss to bulk water and reject high concentration salt back to the beneath water body.

##### 4.1 Reduced Thermal Loss

From the structure point of view, water transportation is realized by an individual sub-component of solar evaporation system. Such component could be integrated<sup>99, 100</sup> in the system as a complete unit or fabricated as a separated part.<sup>101-103</sup> Under sunlight irradiation, water is efficiently draw to the photothermal area for evaporation. Inevitably, the thermal energy would flow from the high temperature surface to the low temperature water, resulted in energy transfer, which endowed water for liquid-gas phase transition, or caused the unnecessary energy loss to water body. Hence, in order to take the full potential of solar-induced thermal energy, the design of water transportation is critical. Theoretically, a good balance between vapor production and water transportation is beneficial for efficient thermal energy utilization.

##### 4.1.1 Manipulation of Water Transportation Pathway

Conventionally, in most of cases, the water transportation pathway is integrated with thermal generating layer or self-floating substrate.<sup>104-106</sup> To avoid the direct contact with bulk water, Zhu et al.<sup>62</sup> prepared plasmonic wood (as depicted in Figure 9a) which combined the merits of photothermal nanoparticles and natural wood block for solar vapor generation. The internal hierarchical structure can efficiently pump water to the photothermal layer through capillary effect. Although high light absorption of 98% was achieved by the

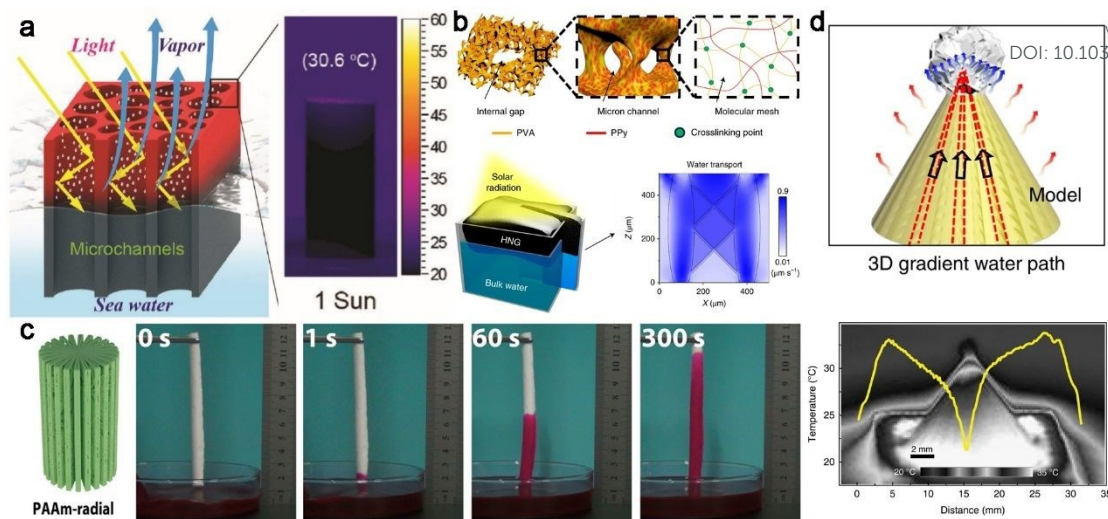


Figure 9 The water transportation manipulated by a) plasmonic wood. Reproduced with permission.<sup>56</sup> Copyright 2018. Wiley-VCH. b) Hierarchical PVA-based gel. Reproduced with permission.<sup>23</sup> Copyright 2018. Springer Nature. c) Hierarchical PAAm-based aerogel. Reproduced with permission.<sup>98</sup> Copyright 2019. American Chemical Society. d) Reversed cone-shaped structures. Reproduced with permission.<sup>29</sup> Copyright 2020. Springer Nature.

plasmonic wood, 30.6 °C of surface temperature and less than 70% of solar energy efficiency was observed under one sun irradiation. Although the carbonized biomass exhibited great promise in low cost fabrication and fast production, the transported water to the photothermal layer might far outweighed the needs for vapor production. The excessive water supply might induce rapid water circulation, resulted in intensified heat exchange and heat loss. To ameliorate the heat convection to water and simultaneously maintained the sufficient water supply for vapor production, water transportation with fine manipulation is required.

Zhao et al.<sup>23</sup> created a hierarchically nanostructured gels which composed of polyvinyl alcohol (PVA) and polypyrrole (PPy) to investigate and pursue the optimal water transportation scheme. With varying weight ratios among PPy, PVA, and water, the inner structure of the gel device changed dramatically, which was critical for efficient water replenishment. With the optimized gel inner structure, composed of internal gaps, micron channels, and molecular meshes (as shown in Figure 9b), a remarkable water evaporation rate of 3.2 kg m<sup>-2</sup> h<sup>-1</sup> under 1 sun illumination was achieved. In addition, the simulation results demonstrated similar water flowing speed across the hierarchical gel, with 0.9 μm s<sup>-1</sup> of bottom water replenishing and 0.89 μm s<sup>-1</sup> of top surface water losing. In this case, energy efficiency of 94% was achieved. Moreover, besides the efficient water replenishment, such remarkable water evaporation rate might also be attributed to the reduced vaporization enthalpy of water confined in gel meshes. Similar hierarchical structure was accomplished by Xu et al.<sup>107</sup>, who inspired by conifer tracheid construction and fabricated an efficient water transportation and evaporation system with polyacrylamide

(PAAm) based aerogel. With the well-defined inner structure, which composed of radially aligned channels, micro pores, and molecular meshes, a long-distance (>28 cm at 190 min) and rapid (>1 cm at 1 s and >9 cm at 300 s) antigravity water transportation was achieved in this work (as shown in Figure 9c), regardless from clean water, seawater, sandy groundwater, or dye-including effluent. Based on the efficient water transportation sub-component, accompanied with carbon heat collector on the top, a solar vapor generation rate of 2.0 kg m<sup>-2</sup> h<sup>-1</sup> and energy utilization efficiency of 85.7% were realized under 1 sun illumination. The impressive water extraction speed exhibited great promise in a broad range of occasions and might benefit for future solar vapor generation with reduced water contact area.

Apart from reducing the thermal loss, the scheme of water transportation could also play positive role in enhancing the vapor generation. Inspired by the super liquid transportation property of the asymmetric capillary ratchet of the bird beak and the pitcher plant peristome surface, Wu et al.<sup>29</sup> designed and fabricated a reversed cone-shaped solar evaporator with asymmetric grooves and microcavity arrays on the surface. Owing to the unique surface design, water was able to move upwardly and spread perpendicularly on the device in merely 100 ms. Consequently, a water film with inhomogeneous thickness along the sidewall was formed, with the apex liquid film thickness of ~15 μm and the bottom liquid film thickness of ~1500 μm. The much thinner liquid film on the apex had higher tendency to be vaporized than the bottom liquid layer, resulted in water evaporation rate of ~0.84 kg m<sup>-2</sup> h<sup>-1</sup> even without solar flux. The position-dependent temperature distribution was another issue to assist the water evaporation. As shown in



Figure 9d, the surface temperature of the evaporator decreased with increasing elevation. Such temperature difference could induce a thermocapillary effect to drive the water upward from the bulk water. With the special water transportation effect and efficient energy utilization on the 3D evaporator, a water evaporation rate of  $2.63 \text{ kg m}^{-2} \text{ h}^{-1}$  was achieved under 1 sun illumination.

#### 4.1.2 Reduced the Water Contact Area

Apart from manipulating the water transportation pathway, reducing the water contact area is proved to be effective in reducing the thermal loss.<sup>108, 109</sup> To narrow down the water transportation pathway, Ni and co-workers<sup>14</sup> created a floating multi-layer solar evaporation device, which composed of solar absorbing fabric as the photothermal layer, expanded polystyrene foam as the floating insulator, and white cellulose fabric as the water transportation pathway (as shown in Figure 10a). The expanded polystyrene with low thermal conductivity ( $\sim 0.02 \text{ W m}^{-1} \text{ K}^{-1}$ ) could limit thermal conduction, whereas the hydrophilic white fabric wick with high thermal conductivity ( $0.58 \text{ W m}^{-1} \text{ K}^{-1}$ ) could leak heat. Thus, in order to localize thermal energy in confined area with efficient water replenishment, a 20% of the wicking area and 80% of insulation area was proposed and resulted in 11% of energy loss by the

pathway. As shown in Figure 10b, due to the structure design, the efficient water replenishment in the aligned GO pillars suppressed the heat dissipation through water convection. As a result, an impressive energy utilization efficiency of 87.5% under 1 sun illumination was achieved. In another example, Ma and co-workers<sup>110</sup> prepared a MOF-based hierarchical system with two side "legs" in the liquid to demonstrate the water evaporation process (as shown in Figure 10c). Owing to the superior hydrophilic feature of the MOF system, water can be efficiently transported to the photothermal layer and cooled the surface temperature from  $56^\circ\text{C}$  to  $31^\circ\text{C}$  in 60s and finally gave a water evaporation rate of  $1.50 \text{ kg m}^{-2} \text{ h}^{-1}$ . A one dimensional water pathway was integrated in a solar evaporator by Yang et al.,<sup>43</sup> as shown in Figure 10e. Due to the reduced contact area toward water, 86.6% of solar energy was utilized for vapor generation with the water evaporation rate of  $1.657 \text{ kg m}^{-2} \text{ h}^{-1}$ . To further narrow down the water contact area, Tu et al.<sup>87</sup> fabricated a black nylon fiber (BNF) flocking board with a water introducing hole ( $5 \text{ mm} \times 5 \text{ mm}$ ) at the middle (as shown in Figure 10d). Owing to the strong capillary effect, a maximum radius of the wetted area was 13.2 cm was observed under 1 sun illumination. Moreover, the corresponding thermal loss driven by the water convection was even lower than that of the air convection.

#### 4.2 Anti-salt Clogging

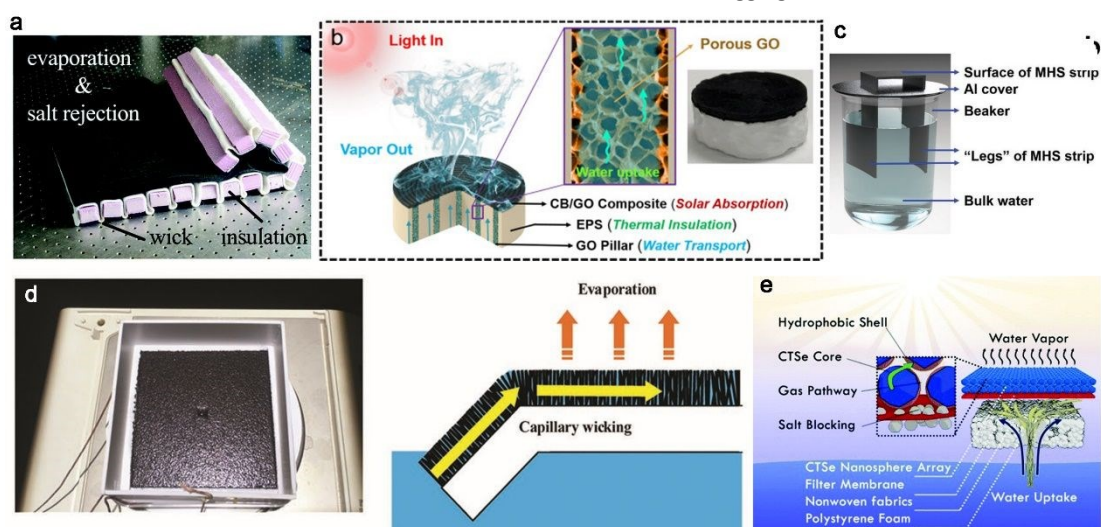


Figure 10 The solar evaporator with reduced water contact area. a) A floating multi-layer solar evaporation device. Reproduced with permission.<sup>14</sup> Copyright 2018, Royal Society of Chemistry. b) A jellyfish-like solar vapor evaporator. Reproduced with permission.<sup>27</sup> Copyright 2017, Elsevier. c) MOF-based hierarchical system. Reproduced with permission.<sup>101</sup> Copyright 2019, Wiley-VCH. d) a (BNF) flocking board. Reproduced with permission.<sup>81</sup> Copyright 2019, Wiley-VCH. e) A hydrophilic/hydrophobic nanoporous double layer structure. Reproduced with permission.<sup>41</sup> Copyright 2018, Royal Society of Chemistry.

water transportation process.

The water contact area was reduced by structure designs. For example, Li and co-workers<sup>27</sup> designed a jellyfish-like solar vapor evaporator with restrained water transportation

Conventionally, the salt crystals can be removed by simply cooling and washing the solar evaporator for several times.<sup>111</sup> However, this strategy may not be appropriated for large-scale operation and has a high risk in increasing the maintaining costs and reducing the long-run productivity. Therefore, solar vapor



evaporators with self-cleaning properties are highly desired.<sup>14, 18, 29, 112</sup> In recent years, in order to address the challenge, several novel strategies have been proposed, including 1) multidirectional mass transfer; 2) Janus structures designs for brine separation; and 3) localized salt crystallization. To some extent, these methods have achieved efficient anti-salt clogging and maintained the solar evaporation functions in long-term operation.

#### 4.2.1 Multidirectional Mass Transfer

Ni et al.<sup>14</sup> fabricated a salt-rejecting evaporation structure with multi-layer configuration. Using diffusion assumption, the area ratio of 1 to 4 between wicking area and insulation area was chosen based on the daily mass of salt to be rejected. As shown in Figure 11a-b, under 1 sun illumination, the evaporation structure was capable to dissolve 40 grams of additional solid salts on the photothermal surface into the underneath brine water, leading to the brine concentration increase from 3.5 wt% to 26 wt%. Although a remarkable salt rejection has been accomplished by this device, the overall solar energy utilization

illumination, salt concentration gradients were formed between micro-sized natural wood channels and mini-sized drilled channels due to their individual hydraulic conductivities. Owing to the hierarchical structure, a mass transfer of salt occurred due to the concentration gradients between the two types of channels via the 1-2  $\mu\text{m}$  pits on the sidewall, resulted in reduced salt accumulation in the system. In addition, the drilled channels with high hydraulic conductivities possessed high potential to exchange with bulk water and functioned as the salt-rejection pathways. Due to the smart structure designs, solar energy efficiency of  $\sim 75\%$  and long-term functions stability was achieved. A similar work done by He et al.<sup>28</sup> applied carbonized balsa wood as the bimodal solar evaporation device. Taking the advantage of the hierarchical and interconnected microstructures of balsa wood, which consisted of large vessel channels (180 to 390  $\mu\text{m}$ ) and narrow tracheid channels (18 to 39  $\mu\text{m}$ ) and micro-sized pits ( $\sim 1$  to 2  $\mu\text{m}$ ) and nanopores on the walls of the microchannels, rapid brine water replenishment and efficient salt rejection were achieved due to the capillary effect and the concentration gradient. However, although the carbonized balsa wood demonstrated efficient salt rejection property, the solar evaporation rate of 0.8  $\text{kg m}^{-2} \text{h}^{-1}$  and energy

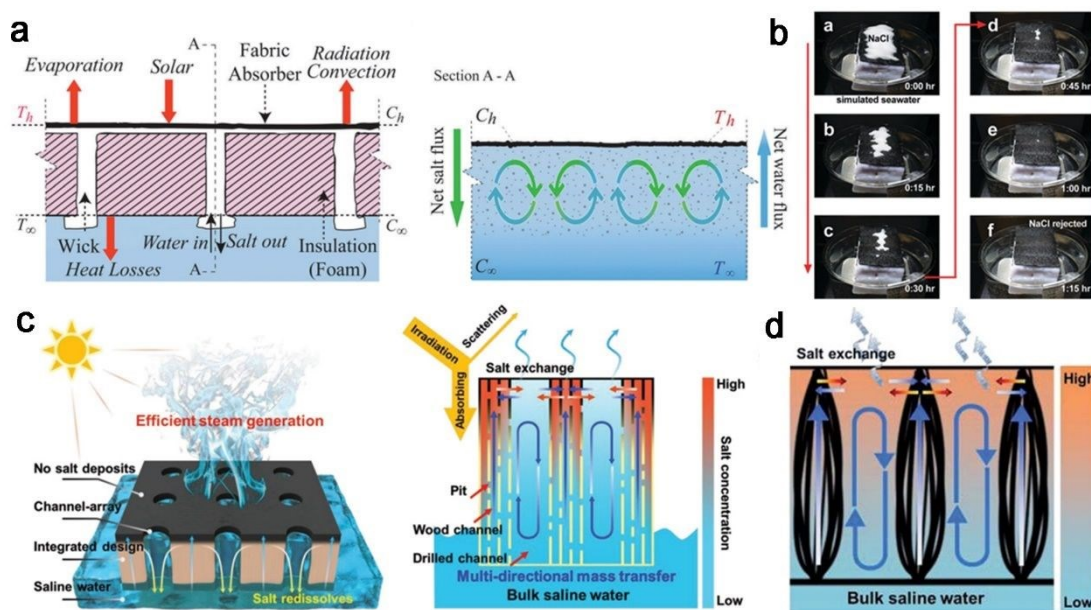


Figure 11 Structure designs for surface salt rejection. a,b) The schematic illustration and performance of the floating multi-layer solar evaporation structure for surface rejection. Reproduced with permission.<sup>14</sup> Copyright 2018, Royal Society of Chemistry. The schematic illustration of multi-directional mass transfer of accumulated salts by c) drilled carbonized wood. Reproduced with permission.<sup>18</sup> Copyright 2019, Wiley-VCH. and d) artificial composite fabric. Reproduced with permission.<sup>104</sup> Copyright 2018, Royal Society of Chemistry.

was  $\sim 56\%$ , resulted from thermal convection loss and light reflective dissipation.

Kuang and co-workers<sup>18</sup> reported a self-regenerating solar evaporator with excellent antifouling features using a rationally designed artificial channel-array in a natural wood for long-term solar vapor generation. As shown in Figure 11c, under sunlight

utilization efficiency of  $\sim 57\%$  appeared insufficient under 1 sun illumination.

Wang et al.<sup>113</sup> applied the hydraulic conductivities difference in an artificial solar evaporation system to achieve efficient anti-salt function. With blank hollow spacer fabric as the template, chitosan as the filler and reduced graphene oxide as the surface

coating, a salt-resistant solar absorber was fabricated. As shown in Figure 11d, due to the aligned big channel array (2 mm) inside the absorber, an efficient salt liquid exchange between porous fiber cluster and big channel occurred, resulted in continuously reducing the salt accumulation. Moreover, due to the porous textile fabric structure, good photothermal conversion and limited thermal conductivity of the solar absorber, an efficient energy utilization of 86% with the evaporation rate of  $1.4352 \text{ kg m}^{-2} \text{ h}^{-1}$  was achieved under 1 sun illumination.

#### 4.2.2 Janus Structures Designs for Brine Separation

To avoid the salt crystallization in solar evaporation device after water evaporation, Zhao et al.<sup>38</sup> proposed a hydrophobic MXene membrane to against liquid infiltration. The non-wettable surface efficiently blocked the brine water underneath and let the generated vapor escaped through the surface gap. A long-term stable solar vapor generation was ensured under 1 sun illumination over 200 hours without noticeable solid deposition. However, the strong hydrophobic may also affect the water supply, and resulted in a solar evaporation rate of  $1.31 \text{ kg m}^{-2} \text{ h}^{-1}$  with solar vapor conversion efficiency of 71%. To address this drawback, Yang et al.<sup>43</sup> further modified the membrane configuration and designed a Janus hydrophilic/hydrophobic double layer for efficient long-term water desalination. The hydrophobic salt-resistant layer of well-defined nanoparticle arrays was served as photothermal layer and vapor pathway, while the hydrophilic filler membrane was served as the brine water replenishment pathway. As shown in Figure 12a, in the Janus configuration, water cannot immerse

10 hours. A layer of salt crystals was appeared on all-hydrophilic systems while the Janus system kept clean and dry. Due to the salt-resistant feature of the Janus double layer and reduced thermal loss in this work, a stable and efficient solar generation was accomplished with the evaporation rate of  $1.657 \text{ kg m}^{-2} \text{ h}^{-1}$ , solar energy efficiency of 86.6%, and long-term stability over 15 days.

Almost at the same time, Xu and co-workers<sup>114</sup> proposed a flexible Janus absorber composed of an upper hydrophobic photothermal layer and a bottom hydrophilic water-supply layer for long-term solar evaporation. Under sunlight illumination, the upper layer can efficiently convert solar energy into heat for water evaporation while block the salt deposition underneath. Hence, the salt deposited in the hydrophilic layer can rapidly be dissolved due to the continuous water pumping. Under 1 sun illumination, an evaporation rate of  $1.3 \text{ kg m}^{-2} \text{ h}^{-1}$  and solar energy efficiency of 72% was accomplished by the Janus system. In addition, the performance of solar vapor generation sustained over 16 days, indicated an excellent salt rejection property and strong structure durability.

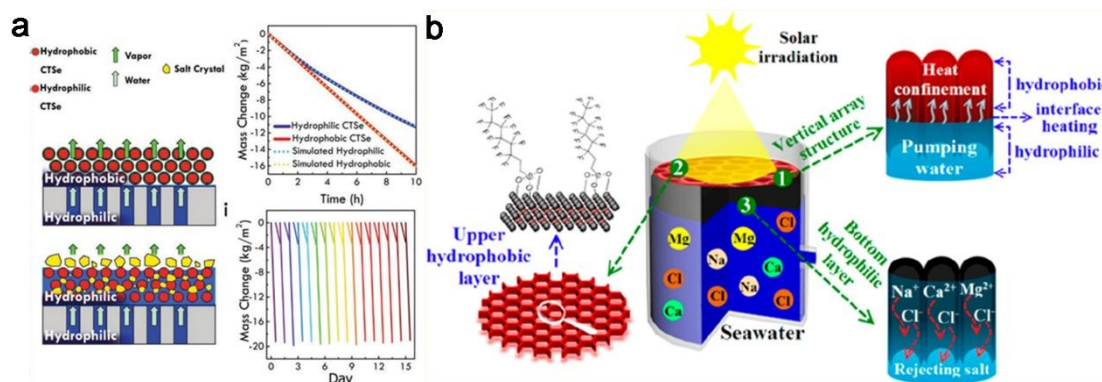


Figure 12 The schematic illustration of Janus membrane and hydrophilic membrane for salt-rejection. Reproduced with permission.<sup>41</sup> Copyright 2018, Royal Society of Chemistry. The schematic illustration of Janus MXene aerogel with well-ordered vertical porous channel for highly efficient long-term solar water evaporation. Reproduced with permission.<sup>106</sup> Copyright 2019, American Chemical Society.

the photothermal layer thus the concentrating process of brine only occurs beneath the hydrophobic layer. In contrast, the all-hydrophilic membrane can be immersed with brine water and precipitated solid salt crystals as the water evaporates. The salt-rejection properties of Janus and all-hydrophilic systems were further compared by illuminated with sunlight for continuous

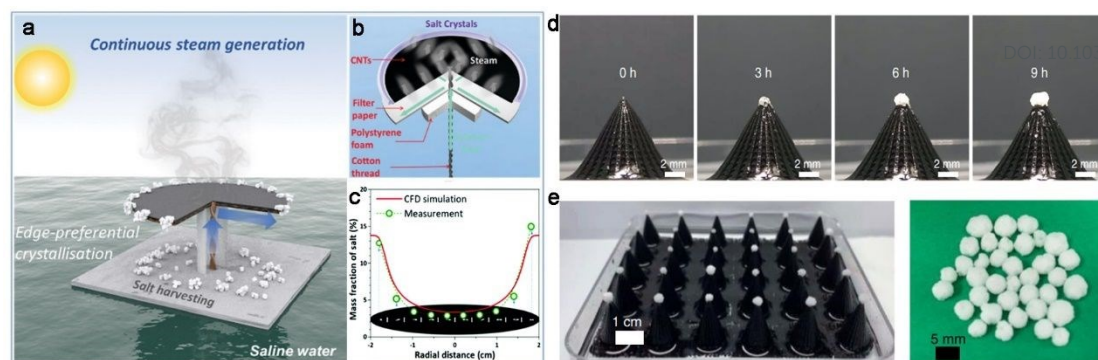


Figure 13 Schematic illustration of a) edge-preferential salt crystallization and b) brine water transportation. c) The mass fraction of salt on the evaporation disc. Reproduced with permission.<sup>17</sup> Copyright 2019, Royal Society of Chemistry. d) The localized salt crystallization of reversed cone-shaped solar evaporator at different time points. e) The solid salt collection by an array of solar evaporators. Reproduced with permission.<sup>29</sup> Copyright 2020, Nature Springer.

Although salt-resistance was achieved by Janus system, the relatively low energy utilization efficiency remained as the major drawback due to the thermal convection loss to bulk water. Although external water pumping components have been proposed to ameliorate this issue, the structure durability problem may bring new concerns. To address these challenges, Zhang et al.<sup>115</sup> designed a vertically aligned Janus MXene aerogel with well-ordered vertical porous channels, selected channel diameters and structure thickness to perform efficient long-term solar vapor generation (as shown in Figure 12b). Compared with irregular porous channels, the well-aligned porous channels exhibited competitive advantage in water transportation, light absorption, and vapor escape. With optimize channel diameter of 15  $\mu\text{m}$ , water transport rate of 0.54  $\text{g min}^{-1}$  was achieved that laid solid foundation for brine replenishment and salt dissolution. In addition, with the structure thickness of 10 mm, a good balance between thermal localization and vapor efficiency was achieved, resulted in the water evaporation rate of  $\sim 1.46 \text{ kg m}^{-2} \text{ h}^{-1}$  and solar energy efficiency of 87%. Furthermore, due to the intact structure of the Janus aerogel, a nearly constant water yield was maintained for 15 days.

#### 4.2.3 Localized Salt Crystallization

Previous efforts have been devoted to reducing the salt concentration inside the solar evaporation system and hence preserved the vapor generation performance in long-term operation. In contrast, localized salt crystallization method offers a new strategy to maintain the continuous vapor production while harvested the solid salts from seawater. Xia et al.<sup>17</sup> designed and fabricated a disc-shaped solar vapor generator that achieved vapor generation and solid salt harvesting at the same time. As shown in Figure 13a-b, the brine water can be efficiently pumped to the evaporation surface and diffused in a radial manner. Under sunlight illumination, salt

was crystallized at the edge location as water evaporated. Figure 13c clearly indicates the salt mass distribution on the evaporator. Moreover, due to edge-preferential crystallization property, the solar evaporation performance remained nearly constant for over 600 hours operation.

Another localized salt crystallization strategy was proposed by Wu et al.,<sup>29</sup> who designed a reversed cone-shaped solar evaporator with bio-mimetic surface structure. As mentioned in section 4.1.1, the super liquid transportation property of the solar evaporator and reversed surface temperature gradient can efficiently transport water from the bottom site to the apex, resulted in the strong vapor production on the top. Consequently, salt is crystallized at the apex with growing diameters as water evaporated, as shown in Figure 12d. In addition, even though solid salt crystals capped the apex, the solar vapor generation remained nearly unchanged, due to the vapor escape channel in the salt crystals. The larger scale salt harvesting and water evaporation is shown in Figure 13e. Took the advantages of water transportation, efficient energy management, and localized salt crystallization, a solar-driven water evaporation rate of  $2.63 \text{ kg m}^{-2} \text{ h}^{-1}$  with energy efficiency of  $>96\%$  was realized by this evaporator under one sun illumination. Such unique structure design offered a new insight for long-term water evaporation and reuse of sea salt harvesting.

## 5. System Designs for Enhanced Water Yield

Water collection is the last but most important step in the solar vapor generation, considering the ultimate goal of freshwater production. However, the previous efforts in this field mainly focus on efficient vapor generation with comprehensive energy management,<sup>116-118</sup> the water collection process has been paid very less attention to. For a typical water collection system, the generated vapor was condensed into water on the transparent titled roof and finally dripped into reservoir with gravity.<sup>119-121</sup>

However, huge discrepancy between the solar-driven vapor generation rate and freshwater collection rate has been found.<sup>23, 122, 123</sup> Table 1 summarize the vapor/water production rate of systems with condensation systems. However, the conventional condensation setup of transparent titled roof could only contribute to low water/vapor ratio (defined as the ratio of the mass of distillate to the mass of the input steam). The big difference in vapor and water production can be ascribed to the optical impedance by the condensed water, absorption of sunlight by the inner vapor, and increased internal humidity as water evaporated. Therefore, creating and developing

Table 1 The water yield of solar-driven evaporation with condensation system

Condensation scheme	Solar absorber		Light intensity (kW m <sup>-2</sup> )	Water evaporation rate (kg m <sup>-2</sup> h <sup>-1</sup> )	Water production rate (kg m <sup>-2</sup> h <sup>-1</sup> )	Water/Vapor ratio (%)	Refs
Titled roof	Carbon Sponge		Natural sunlight	1.15	0.35	30.43	100
	Graphene assembly framework		1	2.1	0.8	38	124
	PVA-rGO hydrogel		1	~2.5	~1.3	52	40
	Cu <sub>2</sub> SnSe <sub>3</sub> /Cu <sub>2</sub> ZnSnS <sub>e4</sub> film		1	1.657	0.889	53.65	43
	CNT-coated conical structure		1	2.63	1.72	65.40	29
	Polypyrrole-modified maize straw		1	3.0	2.2	73.33	125
	Commercial fabric and polystyrene foam		Natural sunlight	Not mentioned	2.5 L m <sup>-2</sup> day <sup>-1</sup>	N/A	14
	Reduced graphene oxide/cotton fabric		1/Natural sunlight	1.47	~4 L m <sup>-2</sup> day <sup>-1</sup>	N/A	126
	PPy functionalized paper		1/Natural sunlight	2.99	~6.9 L m <sup>-2</sup> day <sup>-1</sup>	N/A	15
	Defect-abundant graphene aerogel		1/Natural sunlight	1.78	9.52 L m <sup>-2</sup> day <sup>-1</sup>	N/A	127
	AIE/All-Fiber aerogel		1/Natural sunlight	1.43	10.9 L m <sup>-2</sup> day <sup>-1</sup>	N/A	128
	PVA-PPy hydrogel		1/Natural sunlight	3.2	18-23 L m <sup>-2</sup> day <sup>-1</sup>	N/A	23
	vapor manipulation	PVA-Ti <sub>2</sub> O <sub>3</sub> Hydrogel		1	~3.6	~1.3~3	36.11-83.33
Polypyrrole (PPy) origami rose		1	1.72-2.25	1.52-2.11	88.37-93.77	77	
Latent heat recovery	Two-stage distiller	solar	1	0.98	1.02	1.04	129
	Multi-stage distiller	solar	1	–	3	N/A	26
	Multi-stage distiller	solar	1	5.78	~4.34	75.08	13

innovative designs with efficient gas-liquid transition effects and water collection rate are of paramount importance to unleash the full potential of solar-driven freshwater production.

5.1 Modification of the Condensation Cover

As the place where generate the condensate, there is no doubt that the physical properties and installation parameters of

condensation surface have significant impacts on the water production. In the previous research studies of solar still, scientists have investigated extensively about the properties of condensation surface, including the type of material, surface roughness, installation inclination, shape, transmittance, wiping and vibration of the condensing surface.<sup>21</sup> However, in order to achieve abundant freshwater production, the decisive factor is whether the condensation surface can maintain the continuous high solar flux. A series of plastic materials, such as acrylic,<sup>130</sup> PET,<sup>21</sup> polyesters,<sup>14</sup> and PMMA,<sup>131</sup> possess high solar transmittance, light weight, and low costs, have been applied in



solar vapor generator. During the solar water evaporation, liquid water was formed on the bottom surface of the transparent cover. As shown in Figure 14a, the hydrophobic nature of the PET plastic would significantly reduce the light transmittance due to the surface dangled water droplets. In contrast, the hydrophilic glass,<sup>132</sup> although it is heavy, brittle, and has higher production costs, the continuous excellent light transmittance may result in nearly 30% enhanced water collection rate. Therefore, it is urgent to discover or develop an alternative material for condensation surface with hydrophilic nature, high transparency, light weight, and low fabrication costs.

The productivity of freshwater from a solar evaporation device is also influenced by the temperature difference between the condensation surface and inner vapor. It has been found that with increasing temperature discrepancy across the condensation surface, higher water production was achieved.<sup>48</sup> Therefore, in order to improve the productivity, various cooling methods, including external water flows,<sup>133, 134</sup> external air flows,<sup>135</sup> and enlarged condensation surface<sup>22</sup> have been reported. Inside the solar water evaporation system, the circulation of air mass was increased by keeping up the

temperature difference across the condensation cover and improved the water productivity. According to the authors, the production of water from the evaporation system was enhanced by over five folds by increasing the condensation area from 0.08 m<sup>2</sup> to 0.52 m<sup>2</sup>.

## 5.2 Manipulation of Vapor Pressure

In a closed system, the evaporation and condensation occurred reversibly, following the equation of  $\text{H}_2\text{O}(\text{l}) \leftrightarrow \text{H}_2\text{O}(\text{g})$ . In order to facilitate the vapor production and thereby strengthen the condensation, it is necessary to reduce the vapor pressure and drive the phase transition direction. It has been approved that wind can accelerate the water vapor generation due to the induced surface negative pressure. Liu et al.<sup>20</sup> have studied the effect of wind-driven negative pressure on the vapor generation. With geopolymer-biomass mesoporous carbon composite as the solar absorber, the vapor production rate was examined under 1 sun illumination at different wind speed. Water evaporation rates of 2.85, 5.90, and 7.55 kg m<sup>-2</sup> h<sup>-1</sup> were obtained under 1 sun illumination at wind speed of 1, 2, 3 m s<sup>-1</sup>, respectively. Such values were far exceeding that of natural

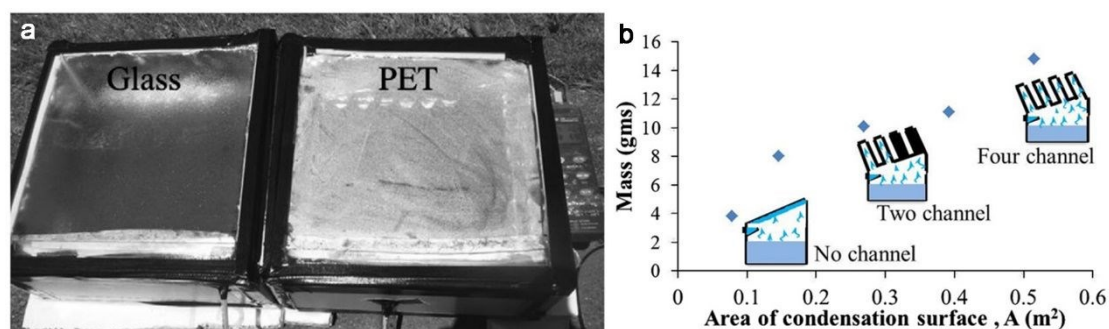


Figure 14 a) The transparency of glass and PET condensation cover during the solar evaporation. Reproduced with permission.<sup>21</sup> Copyright 2013, Elsevier. b) The effect of condensation surface on the water collection rate. Reproduced with permission.<sup>22</sup> Copyright 2015, Elsevier.

temperature discrepancy between solar absorber and condensation cover. With the reduction of glass cover temperature in the range of 6–20 °C, an improvement of water productivity of 20% has been made in the outdoor experiment. However, cooling condensation cover by flowing water film or air requires additional energy input, which significantly undermines the sustainable and economical nature of solar evaporation. In contrast, enlarging the temperature difference by enlarging the condensation area is an attractive strategy to enhance the freshwater production rate. Bhardwaj et al.,<sup>22</sup> provided a flexible and reliable way to enhance the freshwater production by enlarging the condensation area. As shown in Figure 14b, with additional channels integrated on the evaporation cover, increased amount of vapor was recovered for condensation. To a certain extent, the additional channels can be seen as air-flow condensers, which exacerbated the

water evaporation rate (0.502 kg m<sup>-2</sup> h<sup>-1</sup>) and indicated that the increases in wind speed can efficiently promote the water evaporation rate. Saturated evaporation rate was obtained at high wind speed and under strong solar flux due to the limitation in underneath water transportation. Although an efficient strategy to enhance the water evaporation rate was offered by the authors, the freshwater collection experiment has not mentioned.

Zhang et al.<sup>136</sup> designed and fabricated a simple all-in-one solar distillation device for practical seawater desalination. As shown in Figure 15a, the device is composed of two chambers, including an evaporation chamber and a condensing chamber. Under sunlight exposure, the generated vapor was guided to the condensing chamber by solar-powered electrical fan. Due to the enhance circulation of air mass and air-cooled evaporation

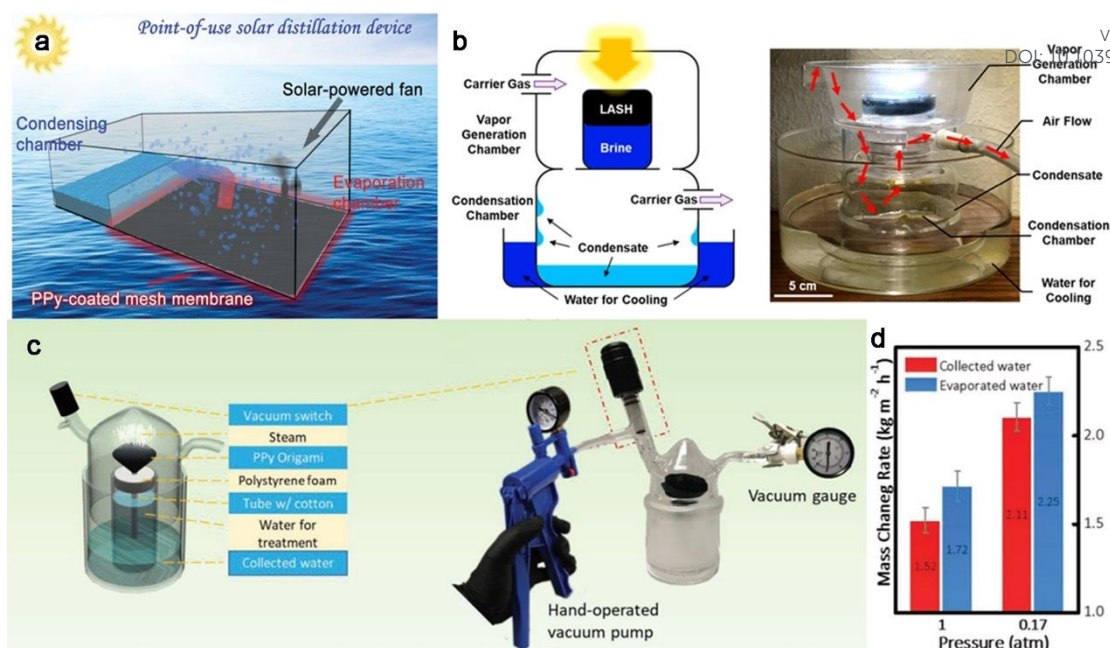


Figure 15 Schematic illustration of water collection by vapor manipulation by a) a simple and all-in-one solar distillation device. Reproduced with permission.<sup>127</sup> Copyright 2015, Wiley-VCH. b) a light-absorbing sponge-like hydrogel with air flow. Reproduced with permission.<sup>19</sup> Copyright 2019, American Chemical Society. and c) low-pressure solar steaming-collection unisystem. d) The performance of vapor and water production under different inner pressure. Reproduced with permission.<sup>77</sup> Copyright 2019, Wiley-VCH.

surface, a water production rate of  $0.15 \text{ kg m}^{-2} \text{ h}^{-1}$  was obtained, which was 15 times higher than that from natural evaporation. Although the water production rate in this work was not promising due to the absence of thermal management scheme, the demonstrated concept provided a direction for vapor manipulation in the early stage of this field.

A more sophisticated solar evaporation system was reported by Guo et al.<sup>19</sup> They fabricated a light-absorbing sponge-like hydrogel which composed of  $\text{TiO}_2$  nanoparticles and PVA chain for highly efficient water evaporation. Due to the energy nanoconfinement and water activation effects, a record high vapor generation rates up to  $\sim 3.6 \text{ kg m}^{-2} \text{ h}^{-1}$  was obtained under 1 sun irradiation in open system. However, the intrinsic water production rate of this system was  $\sim 1.3 \text{ kg m}^{-2} \text{ h}^{-1}$ , due to the rapidly saturated relative humidity, which significantly inhibited the vapor production from the hydrogel system. To overcome this obstacle, airflow was introduced to transport the generated vapor from the evaporation chamber to the condensation chamber to reduce the vapor pressure (as shown in Figure 15b). With the aid of pump, as the speed of air flow increased from 0, to 10, and to 40  $\text{ml min}^{-1}$ , water delivery rate was increased from  $\sim 1.3$ , to 2.2, and  $\sim 3 \text{ kg m}^{-2} \text{ h}^{-1}$ , respectively. The enhanced water production rate was attributed to the reduced humidity induced by the negative pressure. Similar work has been reported by Li et al.,<sup>77</sup> who utilized a low-pressure solar steaming-collection unisystem to reduce the vapor pressure inside the evaporation system (Figure 15c). As shown in Figure

15d, under the reduced pressure of 0.17 atm, the water evaporation rate and water collection rate hugely promote from 1.72 to  $2.25 \text{ kg m}^{-2} \text{ h}^{-1}$  and 1.52 to  $2.11 \text{ kg m}^{-2} \text{ h}^{-1}$ , respectively, compared to ambient pressure.

Although the water production rate was significantly enhanced by reducing the vapor pressure, the energy consumption in this system has not mentioned, thus the capability of the device for freshwater production cannot be fully evaluated. As claimed by Li et al.,<sup>77</sup> such design may be appropriated for portable application in emergency. For large scale solar water evaporation, novel designs with efficient vapor manipulation are urgently needed for sustainable and economical efficient freshwater production.

### 5.3 Latent Heat Recovery

When condensing water vapor by the transparent cover, a large amount of latent heat was discharged into the ambient. Such process occurs regardless of the sunlight absorption capability of solar absorbers and the comprehensive thermal insulation schemes used for water evaporation. Further recovery and utilization of the latent heat could hugely enhance the freshwater productivity.<sup>137</sup> However, it seems impossible to harvest the dissipated latent heat by the typical configuration of solar-driven evaporation system. Photothermal membrane distillation (PMD) system, with the reversed configuration of feed water and generated vapor, exhibited great potential to

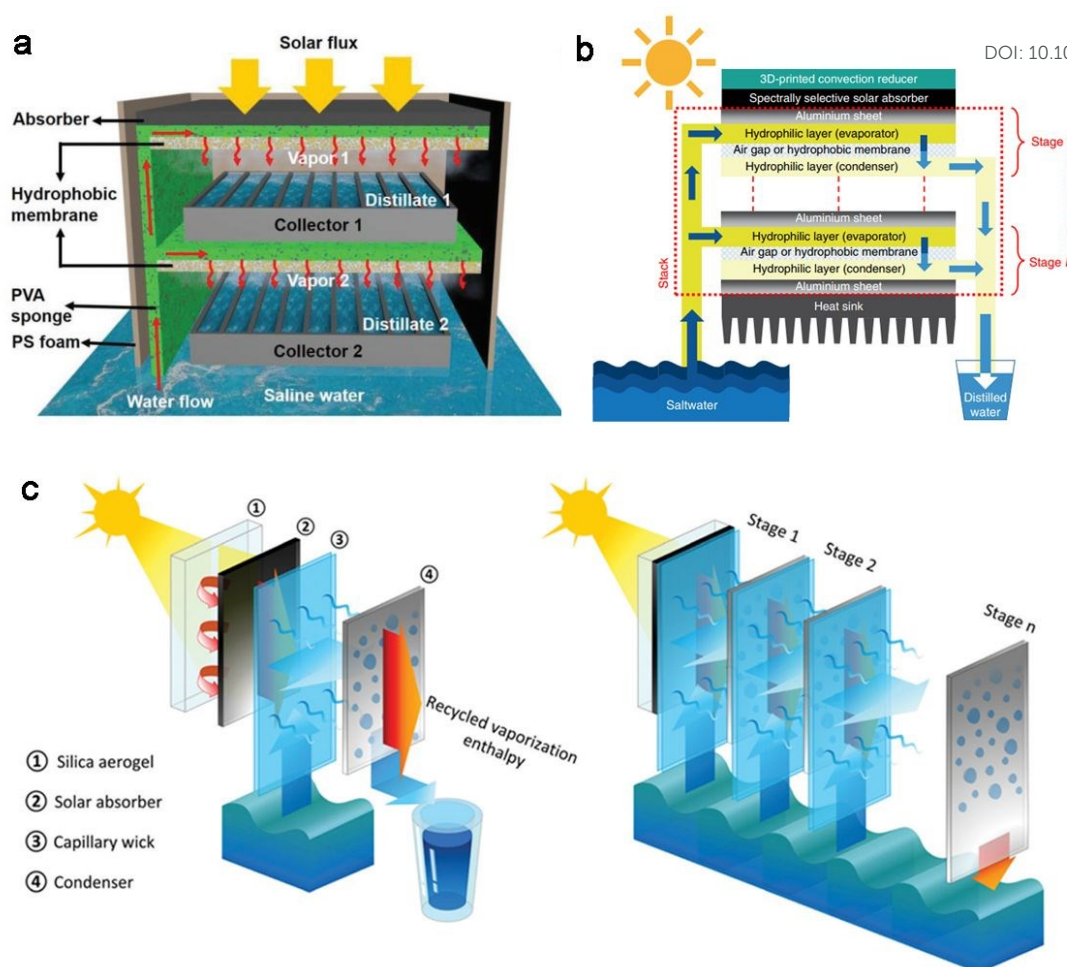


Figure 16 Water yield enhancement by latent heat recovery. a) The schematic illustration of two-stage latent heat recovery device. Reproduced with permission.<sup>123</sup> Copyright 2018, Wiley-VCH. b) The schematic illustration of multiple stage latent heat recovery device. Reproduced with permission.<sup>26</sup> Copyright 2018, Nature Springer. c) The schematic illustration of another multiple stage latent heat recovery system and the detailed device configuration. Reproduced with permission.<sup>13</sup> Copyright 2020, Royal Society of Chemistry.

recover latent heat. PMD is a thermally activated separation process which the separation is driven by phase transition. A hydrophobic membrane/layer is applied to inhibit water transportation but only allowing vapour to go through it. Such process is driven by a partial vapour pressure difference across the hydrophobic layer along with solar-to-thermal generation. In the typical configuration of PMD system, the feed side of liquid water source is located on the hydrophobic membrane, while the vapor is condensed on the opposite side after penetrating the membrane. Compared to solar-driven evaporation scheme, PMD may also has natural advantages in salt rejection and anti-fouling.

Hence, Xue et al.<sup>129</sup> firstly proposed a compact solar-thermal membrane distillation system with the features of localized solar-thermal heating, effective cooling, and latent heat recovery. The evaporation system was composed of a commercial solar absorber (Bluetec, Germen) for heat generation, PVA sponge for seawater transportation,

hydrophobic membranes for antifouling, two metal collectors for vapor condensation. As shown in Figure 16a, with solar light as the only energy input, water evaporation and condensation are occurred sequentially in Collector 1 and Collector 2, which indicates the re-utilization of the latent heat. The temperature of the internal vapor and water collector in two stages are shown in Figure 16b, which well evidenced the energy propagation and recycling. Owing to the novel energy management strategy, a water collection rate of  $1.02 \text{ kg m}^{-2} \text{ h}^{-1}$  with a solar efficiency of 72% was obtained under 1 sun illumination, whereas the vapor generation rate of  $0.98 \text{ m}^{-2} \text{ h}^{-1}$  was achieved in the open system.

Similar but elaborated system was proposed by Chiavazzo et al.<sup>26</sup> They designed and fabricated a passive multi-stage and low-cost solar distiller to recover the phase transition latent heat for enhancing the freshwater yield. Each unit stage for distillation was composed of two hydrophilic layers and an intermediated hydrophobic microporous layer. As the heat-induced vapor



generated from the first hydrophilic layer and condensed in the second hydrophilic layer, the latent heat was recovered as the secondary thermal source to activate another around of vaporization in devices with multilayer configuration. Hence, a stage number dependent water productivity has been confirmed. Specifically, the 3-stage and the 10-stage configuration exhibited a threefold and a six-fold higher water productivity than the single-stage configuration in the laboratory experiments. Owing to the latent heat recovery strategy, an impressive water collection rate of  $3 \text{ L m}^{-2} \text{ h}^{-1}$  was accomplished by the 10-stage configuration device under 1 sun illumination.

Xu and co-workers<sup>13</sup> further elaborated the designs of the multi-stage architecture by adjusting the structural parameters with simulation outcomes. As shown in Figure 16c, the multi-stage architecture is composed of a solar absorbing stage and numbers of evaporation/air/condensation stage. The width of the device  $a$ , the air gap distance  $b$  between the evaporation and condensation membrane, and the total number of stages  $n$  were proved to be of great significance in water and vapor transportation and thermal energy dissipation. In order to maximize the practicability, a trade-off between theoretical performance and practical limitations has been made, which resulted in the configuration of  $a = 10 \text{ cm}$ ,  $b = 2.5 \text{ mm}$  and  $n=10$ . Eventually, the designed multi-stage solar distiller exhibited a record-high freshwater production rate of  $5.78 \text{ L m}^{-2} \text{ h}^{-1}$  with solar-to-vapor conversion efficiency of 385% under 1 sun illumination, which evidenced an efficient latent heat recycling and re-utilization. However, the single-stage configuration only gave a water production rate of  $1.21 \text{ L m}^{-2} \text{ h}^{-1}$  with solar-to-vapor conversion efficiency of 81%, under 1 sun illumination. In general, the latent heat recovery strategy leads to totally different system configurations to the interfacial solar evaporation models, however, with remarkably high energy re-utilization. The significance of multi-stage device is more than a novel way to improve the freshwater productivity, but more importantly, it sheds the new light on the solar water evaporation field and paves a steady step for the future commercialization.

## 6. Recent Progress in Applications

With the ever-deepening of research in solar-driven vapor generation, various novel solar-absorbing materials, comprehensive structure designs, and sophisticated energy management schemes have been proposed to mature the solar evaporation devices and promote the system performance, which laid solid foundation for the future applications. Despite of the nature of energy sustainability and environment friendly, the solar vapor generation still exists unignorable limitations and drawbacks in current stage, such as low freshwater productivity, large footprint requirement, and weather-dependent performance. Nevertheless, in recent years,

scientists have put forward many profound and interesting ideas based on the mass and energy transfer and transformation within the solar evaporation, including seawater desalination,<sup>138-140</sup> sewage purification,<sup>84, 141, 142</sup> and even electricity generation.<sup>112, 143</sup> To some extent, these ideas serve as a guiding role to lead the future solar-evaporation-based applications and enrich the development possibilities. In this section, we review the cutting-edge solar evaporation applications and discuss the underlying mechanism and application potentials.

### 6.1 Seawater Desalination

Considering the ultimate goal of alleviating the water scarcity issue, solar-driven water treatment methods have exhibited great potential in freshwater production for its the unlimited energy and water resources,<sup>144</sup> minor environmental impact, long-term and automatic operations. Compared to the current membrane-filtering technologies, solar-driven evaporation is less susceptible to the quantity and quality of water source and thus is capable to produce clean water from diverse situations, including seawater,<sup>145</sup> household sewage, and industrial wastewater<sup>146</sup> in a cost-efficient way. However, conventional solar-driven water production solutions suffered from low energy utilization efficiency<sup>147</sup> and high capital construction costs,<sup>83, 148</sup> which significantly impeded their development and practical applications.

In the recent few years, due to the drastically changes in the mindset of energy utilization, from volumetric bulk heating,<sup>149, 150</sup> to interfacial heating,<sup>151</sup> and to isolation localized heating,<sup>29</sup> the energy efficiency of solar still type of systems increased dramatically and paved a steady step for the future practical applications.<sup>10</sup> Currently, numerous solar-evaporation devices with enhanced solar evaporation efficiency, salt rejection property, miniaturized structures, and affordable costs were reported. For example, Zhou et al.<sup>40</sup> demonstrated a hydrogel-based solar evaporator with a high energy efficiency of ~95% under one sun for solar desalination (Figure 17a). The solar evaporation hydrogel was prepared by in situ gelation of polyvinyl alcohol (PVA) with the loading of reduced graphene oxide (rGO). Upon sunlight irradiation, the internal PVA hydrogel network can efficiently transport water and confine the thermal energy generated by the embedded rGO, enabling a steady water production rate of  $\sim 1.3 \text{ kg m}^{-2} \text{ h}^{-1}$  under one sun illumination in a closed system. The desalination effect of the solar evaporation device was further examined by testing a real seawater sample (from the Gulf of Mexico) and three artificial seawater samples with representative salinities of the Baltic sea (0.8 wt%), world ocean (3.5 wt%), and Dead sea (10 wt%). As shown in Figure 17b, the concentration of primary ions was measured by inductively coupled plasma spectroscopy (ICP) and the results indicates that the salinity of the condensed water is nearly four orders of magnitude lower than the initial solution,



and two orders of magnitude lower than the drinking water standards defined by World Health Organization (WHO, 1 %) and the US Environmental Protection Agency (EPA, 0.5 %). In addition, the function stabilities of the device were verified under 1 sun illumination for over continuous 96 hours without noticeable change, indicating the excellent durability for long-term practical applications.

The unit cost of water production is another important issue in solar-driven seawater desalination. Ni et al.<sup>14</sup> reported a floating multi-layer solar evaporation structure for practical solar desalination. The flexible assembling materials made this system easy to be deployed for desalination in off-grid and remote areas. In the outdoor experiment, the floating solar still on the ocean (Pleasure Bay, Boston, USA) can produce freshwater at  $2.5 \text{ L m}^{-2} \text{ day}^{-1}$  with the solar-to-water efficiency of 22%, which was enough to satisfy the daily individual drinking needs. As shown in Figure 17c, the materials cost of the entire solar evaporation system was  $\sim \$3 \text{ m}^{-2}$ , which was 10-100 times lower than the current solar still systems. Moreover, with an estimated life cycle of 2 years, the unit cost of water production was nearly  $\$1.5 \text{ m}^{-3}$ , 10 times lower than that of conventional solar still devices. Although current plant-based membrane-filtering water desalination possessed lower unit cost ( $\$0.5 \text{ m}^{-3}$ ), the high capital funding inhibited its operation in remote water-stressed and disaster-stricken communities.

Beyond purifying the seawater for drinking use, the solar water evaporation could also shed new light on the development of marine agriculture. Wang and co-workers<sup>152</sup> designed and fabricated a floating transparent device with multiple horizontal grooves and special interior structure. As shown in Figure 17d-e, the parabolic-shaped surface can efficiently concentrate solar light to thermalize the seawater absorbing material for water

evaporation and the side chamber can condensate the hot vapor to generate freshwater for crops irrigation. Under  $1000 \text{ W m}^{-2}$  irradiation, the water production rate of the proposed floating device was calculated as  $195.1 \text{ g m}^{-2} \text{ h}^{-1}$  with the energy efficiency of 16.5%. The performance of water production rate was relatively low possibly due to the absence of thermal energy management scheme. However, the concept proposed by Zhang et al. may enrich the possibility of applications based on solar-driven desalination.

## 6.2 Sewage Purification

Although ocean possess the most abundant water resource for freshwater generation, in the daily life, household sewage and industrial wastewater have a more intimate relationship with human activities. Various contaminants, including heavy metal ions,<sup>146</sup> organic compounds,<sup>153</sup> oil and grease,<sup>110</sup> and bacteria<sup>154</sup> in the wastewater exhibited severe toxicity not only to the living species but also to the environment. In this age, how to recycle and revitalize the clean water resource from the contaminant water is a widely concern problem. Currently, solar water evaporation may provide an effective solution to deal with this issue by separating and condensing the water vapor under sunlight illumination.

Based on the promising solar-thermal response of graphene, Zhang et al.<sup>124</sup> fabricated a housing self-supply water system with highly vertically ordered pillar array framework (HOPGF). With well-defined structures, a solar vapor generation rate of  $2.10 \text{ kg m}^{-2} \text{ h}^{-1}$  with energy efficiency of 95% was achieved under 1 sun illumination in an open system. The HOPGF was firstly examined to purify seawater and raw pharmaceutical wastewater (acid, alkaline, and neutral solutions) and the

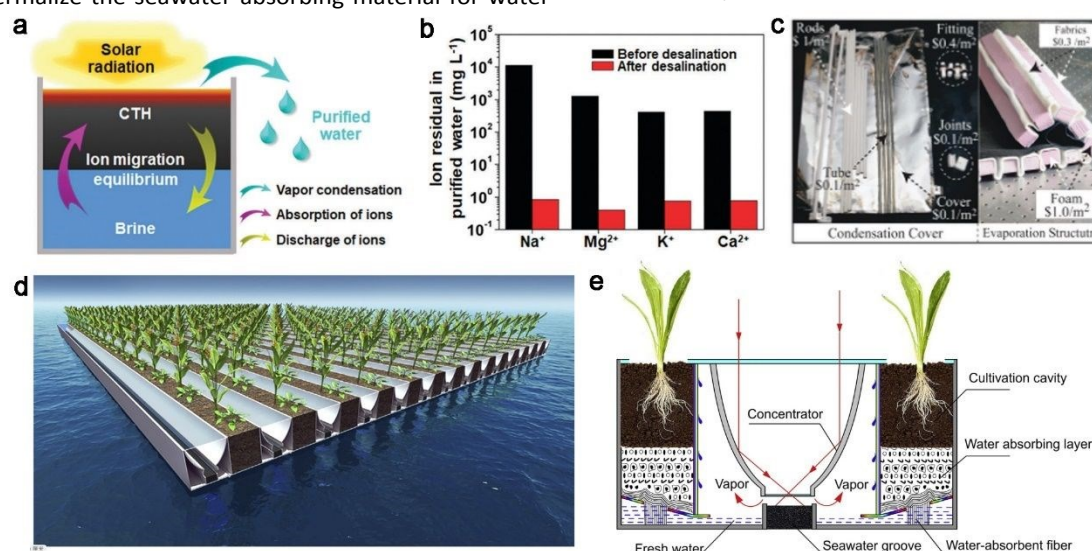


Figure 17 The schematic illustration of a) hydrogel-based seawater purification. b) The ions concentration before and after desalination. Reproduced with permission.<sup>38</sup> Copyright 2018, Royal Society of Chemistry. c) The illustration of the fabrication costs of the floating solar still. Reproduced with permission.<sup>14</sup> Copyright 2018, Royal Society of Chemistry. The schematic illustration of d) marine agriculture accomplished by floating transparent device and e) the freshwater production process. Reproduced with permission.<sup>138</sup> Copyright 2018, Elsevier.

collected purified water was measured with neutral pH and low conductivities. Based on the capabilities of HOPGF, the authors designed and proposed a proof-of-concept housing self-supply water system to realize cyclic utilization of household sewage. As shown in Figure 18a, HOPGF arrays are fixed under the transparent rooftop to acquire efficient solar energy for water evaporation. The household wastewater was drawn to the solar absorber by cotton threads through capillary effects and the hot vapor was condensed on the glass rooftop. According to Figure 18b-c, even under moderate solar flux of 0.6 sun and ambient temperature of 15 °C, an average water production rate of 0.8 kg m<sup>-2</sup> h<sup>-1</sup> was achieved by this system. Moreover, according to the authors, for a building with a roof area of 100 m<sup>2</sup>, 480 kg clean water can be collected in a day, which was sufficient to satisfy the daily needs of seven people. Hence, the proposed housing self-supply water system exhibited great promise to realize cyclic utilization of household sewage for future domestic applications.

To acquire the clean water from industrial sewage, Zhou et al.<sup>89</sup> introduced a highly hydratable light-absorbing hydrogel to achieve efficient water evaporation. According to the authors, enhancing the hydratability of the hydrogel can change the water state and partially activate the water for evaporation, resulted in a water evaporation rate of ~3.2 kg m<sup>-2</sup> h<sup>-1</sup> with an energy efficiency of ~92% under 1 sun irradiation. Based on such impressive performance of solar evaporation, the hydrogel device also exhibited excellent wastewater purification results.

obtained in strong acid (1M H<sub>2</sub>SO<sub>4</sub>) and alkali (1M NaOH) solutions, and the purified water appeared neutral pH. In addition, a nearly four orders of magnitude lower heavy metal ions were obtained by the hydrogel device, which were comparable with current commercial purification methods (Figure 18e). Oils and/or other organic compounds were always contained in the real wastewater and may lead to severe fouling problem of the solar evaporation devices. Ma et al.<sup>110</sup> reported a MOF-based solar-thermal water evaporator to against the organic contaminants in the wastewater. Owing to the strong hydrophilic property of the hierarchical MOF structure, the oil contaminant can be efficient repelled. The Janus feature is indicated by Figure 18f. As shown in Figure 18g, the water evaporation performance was nearly constant in water with oil layer and slightly reduced in the oil-in-water emulsion, compared to clean water.

The combination of photothermal and porous structure could provide new insights on sewage treatment. For example, Lou et al.<sup>153</sup> reported a paper-based composites which composed of reduced graphene oxide (rGO) sheets, porous air-laid paper, and titanium dioxide (TiO<sub>2</sub>) nanoparticles for multifunctional solar-driven clean water generation. As shown in Figure 18h, with the porous structure of the paper substrate and enhanced photothermal response of rGO, contaminants can be efficiently removed through physical absorption with the aid of evaporation-based upward diffusion. Furthermore, taking the advantage of photothermal effects and localized pollutant

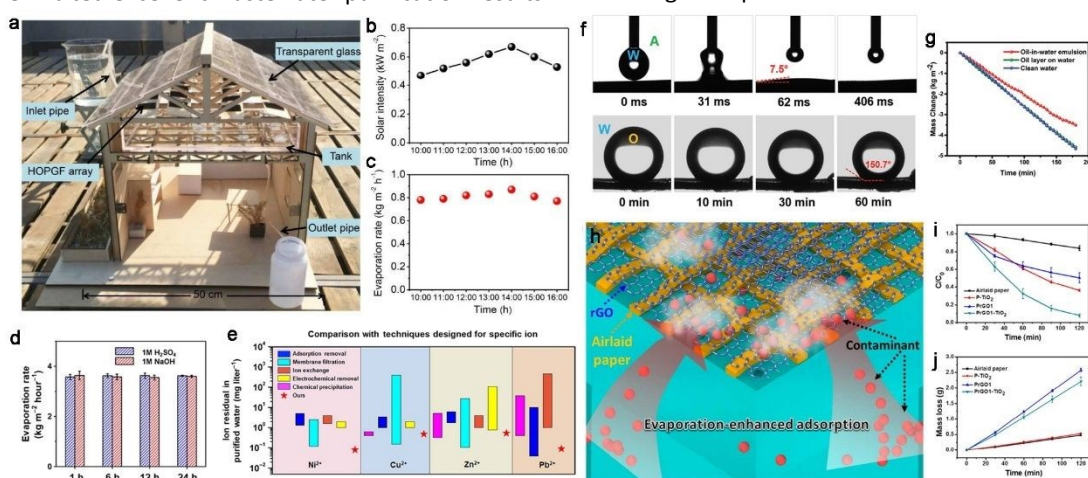


Figure 18 a) The prototype model of a housing self-supply water system. b) The intensity of solar flux at different time points and c) the corresponding water evaporation rate. Reproduced with permission.<sup>141</sup> Copyright 2018, Royal Society of Chemistry. d) The performance of water evaporation in strong acid and alkali. e) The comparison of the heavy metals rejection by the hydrogel system with other commercial approaches. Reproduced with permission.<sup>142</sup> Copyright 2019, American Association for the Advancement of Science. f) The water contact angle analysis indicated that the MOF-based evaporator exhibited strong hydrophilic property. g) The water evaporation rate of the MOF-based evaporator in oil-contaminated wastewater. Reproduced with permission.<sup>101</sup> Copyright 2019, Wiley-VCH. h) The schematic illustration of solar-thermal based decontamination with evaporation-enhanced physical adsorption and photocatalytic degradation. i) The performance of photocatalytic degradation of RhB with solar evaporators with different configurations. j) The water evaporation rate of solar evaporators with different configurations. Reproduced with permission.<sup>139</sup> Copyright 2016, American Chemical Society.

As shown in Figure 18d, steady water evaporation rate was accumulation, a highly efficient photodegradation of

rhodamine B (RhB) in water was accomplished by the embedded TiO<sub>2</sub> nanoparticles. As shown in Figure 18i-j, over 95% of the RhB in the solution was removed by the composite paper under solar illumination for 2 hours and the integration of photocatalytic components only exhibited 10% lower water evaporation rate, which indicated a feasible combination in this work. Moreover, after 4 hours treatment by the composited paper, both the condensed water and purified water appeared colourless and share the same absorbance spectra, which indicated an excellent decontaminant property.

### 6.3 The Evaporation-Assisted Electricity Generation

The innovative designs which tackle two global challenges, freshwater and energy scarcity, under sunlight irradiation exhibited great value to human society. In recent years, the emerging of interfacial solar evaporation offered the new insights on electricity generation. Due to the heat confinement configuration, ameliorated surface temperature,<sup>85</sup> relatively facile preparation processes,<sup>155</sup> and versatile deployable features,<sup>156</sup> the solar water evaporation can be applied in a broad range of occasions with higher energy utilization efficiency. Recent advances demonstrated the evaporation-assisted electricity generation,<sup>157</sup> which based on the physical changes in the evaporation system under sunlight illumination, including temperature difference across the solar evaporator, salinity accumulation beneath the solar absorber,<sup>158</sup> frictional contact induced by downward water flowing,<sup>156, 159</sup> and

horizontal water flow<sup>160</sup> in the evaporation surface, etc. It should be mentioned that the evaporation-assisted electricity generation is not comparable to photovoltaic (PV) technology, however, as an extra bonus, the evaporation-assisted electricity can partially ameliorate the energy scarcity in a humble way. In this section, the conceptual ideas for the dual generation of freshwater and electricity are reviewed.

Previously, numerous research studies focused on enhancing the vapor generation and water production rate under solar illumination were reported. However, the internal enthalpy of steam was usually lost to the ambient as vapor condensed to water, resulting in a huge energy loss. To acquire and re-utilize this part of energy, Li et al.<sup>161</sup> introduced a novel concept to generate clean water and electricity simultaneously by storing and recycling vapor enthalpy derived from the solar-driven steam generation. As shown in Figure 19a-c, under light illumination, hot vapor was generated extensively and condensed to produce clean water, while the energy in the vapor was reserved in the thermal storage chamber. The huge temperature discrepancy between the chamber and ambient environment was utilized to generate electricity by using the thermoelectric modules. Under optimal situation, the solar energy utilization efficiency for vapor generation reached 72.2% and electricity generation reached 1.23%. Such performance was sufficient for the operation of an electric fan and 28 light-emitting diodes. Different from generating electricity by hot vapor, the thermalized solar absorber can induce thermoelectricity directly.<sup>162</sup> As shown in Figure 19d-e, sponge type

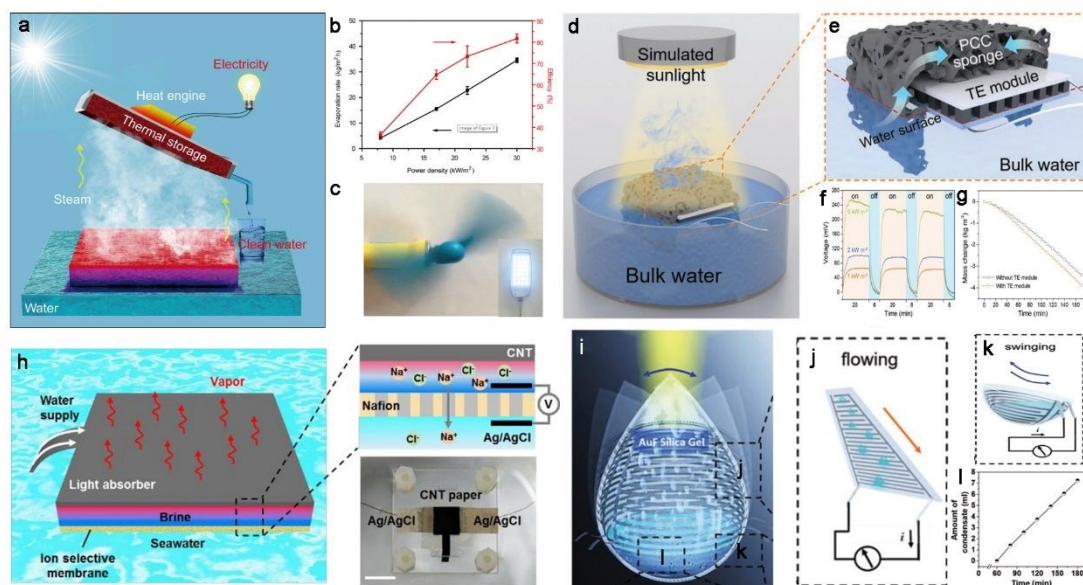


Figure 19 The schematic illustration of solar evaporation accompanied electricity generation. a), d) and e) illustrated the thermal electricity based on hot vapor and thermalized solar absorber. The performance of the dual-functional devices is demonstrated in b), c), f), and g). Reproduced with permission.<sup>149</sup> Copyright 2018, Elsevier. Reproduced with permission.<sup>150</sup> Copyright 2019, Wiley-VCH. h) The electricity induced by salinity gradient across the Nafion membrane. Reproduced with permission.<sup>146</sup> Copyright 2017, Elsevier. i) and j) The schematic illustration of harvesting the triboelectric energy via the downward flow of condensate droplets. k) The wind energy can be harvested due to the swinging of device. l) The water collection amount was recorded with time being. Reproduced with permission.<sup>144</sup> Copyright 2018, Wiley-VCH.



solar evaporator is directly placed on the TE module, which generate electricity based on the Seebeck effect triggered by the temperature discrepancy between the illuminated sponge and bulk water. As shown in Figure 19f-g, with the optimal external resistance of 2  $\Omega$ , a maximum output power density of 0.4 W m<sup>-2</sup> was achieved under 1 sun irradiation. Notably, the coupling of solar evaporation and thermo-electric technologies was realized without trade-offs, with evaporation efficiency of 87.4% under 1 sun illumination.

Apart from the thermal generation, the salinity difference induced by water evaporation has also been applied for electricity generation. Yang and co-workers<sup>158</sup> proved that salinity difference between evaporation accumulated liquid and seawater can be utilized for electricity generation. The authors prepared a hybrid system which composed of a carbon nanotube (CNT) modified filter paper and an additional ion selective membrane (Nafion membrane) to generate water vapor and ions gradient at the same time. As shown in Figure 19h, as water continuously being evaporated, high concentration salt water is confined in a limited space between the CNT paper and Nafion membrane for electricity generation. The water evaporation and electricity generation increased with enhanced solar power and maximum water evaporation rate of 1.1 kg m<sup>-2</sup> h<sup>-1</sup> and electricity power of ~1 W m<sup>-2</sup> were achieved under one sun illumination.

Taking the advantage of the downward flow of condensate droplets, Gao et al.<sup>156</sup> fabricated a proof-of-concept prototype to collect the condensation water and to harness triboelectric energy at the same time. As shown in Figure 19i-l, the prototype consists of inclined walls and a round bottom vessel (lined with PTFE energy harnessing triboelectric nanogenerator (TENG) devices), and water evaporator hydrogel. Under sunlight illumination, the generated vapor was condensed on the tilted walls as tiny water droplets and further grew bigger and flew down to the collection vessel with gravity. The flow of the water droplets generated electricity due to the electrification of the water and the PTFE, which resulted from negatively charged of PTFE and positively charged of water droplets. Moreover, wind energy, which can affect the flow condition of condensate droplets and electrification of the prototype system, can also be harvested. According to the authors, the maximum peak power obtained by this system was 0.63  $\mu$ W with the evaporation efficiency of ~85% under one sun illumination.

Electricity generated from the evaporation-driven water flow was recognized as a newly developed green energy in recent years.<sup>163</sup> Xiao and his co-workers<sup>160</sup> proposed a novel concept to realize an efficient combination of solar evaporation and horizontal water-flow-induced power generation by an asymmetric functionalized Janus material. The dual-functional solar evaporation device was composed of a bilayer carbon nanotubes (CNTs)/cellulose paper with partially covered by hydrophobic polydimethylsiloxane (PDMS) on the bottom. Due

to the confined water flow in the membrane device, the directional protons flow enabled the electricity generation. It was proved that the ion concentration, solar light intensities, and load resistance significantly all affected the power generation. In the optimal situation, a maximum output power of 2.1  $\mu$ W and 1.15 kg m<sup>-2</sup> h<sup>-1</sup> was accomplished by the Janus device under one sun illumination.

Solar-driven evaporation is a process which involved with multiple physical changes, such as thermal generation, salinity gradient enhancement, condensation of vapor, and water transportation. Taking the advantage of those processes may help to produce extra electricity energy. It has to accept that the productivity of evaporation-assisted electricity is far lower than PV technology (about 1 or 2 orders lower). However, the electricity generation is accompanying with solar-driven evaporation as a by-product but not as the main product. The innovation designs of dual-functional solar-driven evaporation provides a feasible pathway to ameliorate water and energy scarcity at the same time. However, the previous mentioned research works in this section are mainly accomplished in the indoor environment, which may not have strong enough reliability to sustain the same performance in the practical application.

## 7. Conclusion and Outlook

### 7.1 Conclusion and Discussion

Solar evaporation strategy has become one of the most potential technologies to tackle water scarcity over the past several years. The previous reports focused on the thermal-driven water evaporation with the photothermal conversion and utilization as the main direction.<sup>31</sup> Thus, great strides have been made in the design and fabrication of solar absorbers and achieved remarkable vapor production rate in open system.<sup>20, 23</sup> However, the solar evaporation is a pluralistic process, involving energy absorption and manipulation, water transportation, and water collection. The freshwater yield, as the ultimate goal, is more direct metrics for the performance evaluation of solar distillers.

Recent advances in solar evaporation reveal the significance of the system designs of functional modules on the overall performance enhancement. The energy absorption is considered as the foundation for water evaporation. In order to enlarge the total energy input to the solar-driven evaporation device, modification of surface topography, energy concentration scheme, and gaining environmental energy strategies have been summarized in this review article. These proposed strategies have all demonstrated positive effects in enhancing water evaporation rate. Specifically, by modifying the surface structures, solar absorber is capable to minimize the

light reflection and compensate the variation of solar angles, which strengthen the solar absorption. Such design is especially beneficial for all-day long solar-related applications. We envision huge potential of this strategy, since the performance enhancement can be achieved by other devices by simply coping the designed surface pattern. Motivated by optical concentration method, thermal concentration scheme was proposed to achieve high temperature (100 °C) vapor under natural sunlight. Previously, efforts were devoted to increasing the interface temperature as much as possible in order to accelerate the water evaporation process. The emerging of thermal concentration scheme shed new lights on thermal-to-vapor conversion. However, the large footprint requirement and intensified heat loss of this scheme, significantly hinder its development in solar evaporation under current system configurations. Nevertheless, we still believe the thermal concentration scheme has huge unexplored potential to be exploit, which requires further development and motivation in research communities. Recovering environmental energy is an efficient method to boost the water evaporation rate beyond the theoretical upper limit. In a typical design for cold vapor generation, elaborated surface structures and intensified vapor escaping are required to realize low surface temperature (below room temperature) of device. In this case, an energy flow from warmer environment to evaporation device occurs, which enlarge the energy input for vapor generation. Although the water evaporation rate can be enhanced significantly by recovering environmental energy, it is of great challenges to condense the cold vapor to boost up the water production rate. Hence, further development is necessary to come up with a solution to address the condensation issue.

Water transportation module plays a significant role in building the connection between solar absorbers and water bodies. However, the water flows across the solar absorber takes most of thermal energy, is considered as the major heat draining pathway. In order to achieve efficient solar evaporation, it is necessary to maintain good balance between the thermal generation and the water transportation. Currently, such goal can be accomplished by either deigning the water supply pathway or reducing the water contact area. For example, Zhao et al.<sup>23</sup> prepared a PVA gel-based evaporation device with hierarchical internal structure for water replenishment, which contributes to 0.90  $\mu\text{m s}^{-1}$  of bottom water transport rate and 0.89  $\mu\text{m s}^{-1}$  of surface water loss rate. Li et al.<sup>27</sup> fabricated a composite evaporation device with jellyfish-like water wicking channels, resulted in reduced water contact area and heat conduction loss. Previous attempts already proven the capability and feasibility of system designs of water pathway in improving the energy utilization and water evaporation rate. Hence, it is of great importance to adopt these concepts in practice. Salt crystallization in solar-driven evaporation system can significantly undermine the performance of water evaporation by increasing the optical reflectance and impeding

water and vapor transportation. To address this challenge, multidirectional mass transfer, Janus structure, and localized salt crystallization method have been proposed in recent two years. Although multidirectional mass transfer and Janus structure have proven to be effective in salt-rejection for a long continuous working period, the adopted system design may compromise the water evaporation rate. Shortly, the multidirectional mass transfer method relies on the difference of salt gradient and hydraulic conductivity to reject salt back into bulk water. Such strategy requires sufficient water exchange between evaporation system and bulk water, resulted in enhanced heat conduction loss. To reject salt accumulation by Janus evaporation system, the thickness of hydrophobic top layer is critical, for which thin layer may not be efficient to against the salt solution infiltration and thick layer may not be efficient to escape water vapor. Moreover, the membrane configuration of Janus structure possesses relatively higher thermal loss. Hence, further improvements are necessary to mature these two strategies before applying in real-world applications. In contrast, localized salt crystallization method, which does not inhibit the salting out behaviour but induce crystallization in desired place, is a promising approach to perform water evaporation without compromise. Moreover, this approach can not only recover the freshwater, but also collect salt crystals as recycle source. Therefore, localized salt crystallization exhibits higher value and potential for commercialization.

Water collection as the final step in solar evaporation process has gained increasing interest recently. In conventional vapor condensation design, gas-liquid transition is performed on transparent titled cover and water is collected by down flow with gravity. However, huge discrepancy between water evaporation rate and water production rate has been found, due to the optical impedance of condensation cover, sunlight absorption by inner vapor, and inner saturated humidity. In order to overcome these obstacles, researchers have provided three strategies to combat the phenomena from different angles. The first strategy to enhance the freshwater yield is to change the structural features of condensation cover. For example, enhance the hydrophilicity of inner cover surface can promote the water film formation and reduce the water droplet, resulted in enhanced light transmittance. Enlarge the area of condensation cover can increase the temperature discrepancy across the cover and hence promote the gas-liquid transition. Currently, glass has proven to be the most effective materials for condensation cover. The structure features mentioned above is feasible to be realized on glass with current technology. However, the fabrication costs and maintaining lifetime are other concerns to be considered. Manipulation of vapor has proven to be highly effective to enhance the freshwater production rate. The introduction of negative pressure can not only accelerate the vapor collection rate, but also promote water evaporation. However, a fact cannot be

ignored is that the negative pressure requires additional energy input. Such energy consumption makes the entire solar evaporation process complex and difficult to be handled, especially in large scale solar distillation. Therefore, further studies are required to balance the energy input and freshwater output and consider the whole process in a comprehensive manner. Very recently, latent heat recovery strategy is reported to enhance the water collection rate by recycling and reutilizing the released latent heat. In conventional system setup, the latent heat energy is dissipated to the environment once the phase transition of gas-liquid occurred on the condensation cover. By reversing the vapor escape direction, the latent heat can be recycled with multi-stage condensation configuration. Remarkably, a record high water evaporation rate of  $5.78 \text{ kg m}^{-2} \text{ h}^{-1}$  and water collection rate of  $\sim 4.34 \text{ kg m}^{-2} \text{ h}^{-1}$  were realized by a 10-stage solar-driven evaporation system.<sup>13</sup> In general, latent heat recovery shed new lights on freshwater production with enhanced energy utilization. Considering the promising performances in solar evaporation, it will be beneficial to adopt this strategy in real-world applications.

## 7.2 Challenges and Perspectives

Regardless of fast and extensive development in the solar evaporation field, they are still multiple challenges that requires further study to bring solar evaporation into practice to real world applications. With the trend of approaching to the commercialization, it is necessary to optimize and balance the issues of freshwater efficiency, environmental impacts, function stability, scalability and fabrication cost of solar-driven evaporation systems.

Recent breakthroughs of system design of solar absorber with comprehensive thermal management scheme have efficiently boosted the water evaporation rate, however, the freshwater obtained from the gas-liquid transition is still in the infant stage. In the previous sections, we have mentioned that cold vapor driven by the environment energy can efficiently upregulate the overall water evaporation rate, with the value far higher than the theoretic limit. However, owing to the intrinsic low temperature of cold vapor, it is difficult to condense them on the condensation cover due to the reversed temperature discrepancy (the cold vapor has lower temperature than the ambient). In contrast, the hot vapor condensation can be easily enhanced by modification of condensation cover, introduction of negative pressure, and recycling of latent heat. However, the fabrication cost of condensation surface, the extra energy input of negative pressure, and the scale up problems in multistage latent heat recovery system may bring new concerns to be overcome.

Given the nearly unlimited solar energy source and diverse water sources, the solar evaporation technology with facile preparation process, low capital investment, zero carbon

Previous efforts of solar distillation were accomplished in laboratory conditions with brine or even pure water as the water sources. However, when considering the practical applications, it is inevitable to face diverse types of water sources, such as seawater, river water, ground water, and industrial and household sewage, which may contains a large amount of uncertain contaminant, such as metal ions, oil and grease, organic compounds, and bacterial. The resistance of these contaminants is essential to maintain the functional and structural integrities of solar evaporators. For example, the fouling by organic compounds may affect the physical property of solar absorber, resulted in reduced water evaporation rate. The high operating temperature may accelerate the corrosion of the solar evaporation device in high salinity water. The salt clogging in the solar evaporators may increase the surface light reflection and limit the water transportation pathways, thus affect the long-term operation productivity. Although great efforts have been made to overcome the fouling by diverse contaminants via material engineering and structural designs and achieved effective results, in most cases, there is a trade-off with the performance of solar distillation. Hence, creating a novel solution to counteract various water sources over a wide range of conditions for long-term high-performance solar evaporation posed a challenging task.

When facing commercialization, the scalability and cost of solar evaporator are two important factors affect the competitiveness of this technology. However, most reported cases did not provide the systematic analysis of cost and mention the scale up potential for real-world implementation. Previous reports payed much more attention to the performance enhancement in water evaporation than the costs analysis. The expenses of raw materials, fabrication and design costs of the solar evaporators, and the lifetime maintaining need to be specified and compared to the existing purification and desalination technologies to promote the acceptance by potential customers. Moreover, previous and current studies mainly focused on the unit performance of solar evaporator, the potential of large-scale solar evaporation has not been evaluated in a quantitative way before. Hence, a greater focus in this aspect is necessary to direct the solar evaporation technology into commercialization. Future research studies for developing new solar evaporation systems should consider more about the cost-effective issue and a systematic analysis method for evaluating the large-scale potential is highly desired.

footprint, and automatic operation is considered as the most promising technology to tackle the water scarcity in this age. Although the current technology remains multiple challenges to



## ARTICLE

## Journal Name

be addressed, we foresee great development of solar evaporation in the coming decade. In order to help the research communities to catch the development trend in this field, we summarize the recent advances in solar evaporation with clear functional partitioning. In addition, we hope this review can help readers quickly hold of the overview of the current solar evaporation technologies and stimulate sparkles of thoughts on the exploration of advanced technologies to tackle water scarcity with unlimited energy and water sources.

## Conflicts of interest

There are no conflicts to declare.

## Acknowledgements

This research is supported by the National Natural Science Foundation of China (No: U1801254, 51925805), the Project of Department of Education of Guangdong Province (No:2018KZDXM060) and Natural Science foundation of Guangdong Province (2019A1515012163), a grant from the Research Grants Council of the Hong Kong Special Administrative Region, China (PolyU 15200518) and The Hong Kong Polytechnic University (G-UAHK).

## Reference:

1. J. Schewe, J. Heinke, D. Gerten, I. Haddeland, N. W. Arnell, D. B. Clark, R. Dankers, S. Eisner, B. M. Fekete, F. J. Colón-González, S. N. Gosling, H. Kim, X. Liu, Y. Masaki, F. T. Portmann, Y. Satoh, T. Stacke, Q. Tang, Y. Wada, D. Wisser, T. Albrecht, K. Frieler, F. Piontek, L. Warszawski and P. Kabat, *Proc. Natl. Acad. Sci.*, 2014, **111**, 3245.
2. J. H. Reif and W. Alhalabi, *Renewable Sustainable Energy Rev.*, 2015, **48**, 152-165.
3. M. M. Mekonnen and A. Y. Hoekstra, *Sci. Adv.*, 2016, **2**, e1500323.
4. M. Elimelech and W. A. Phillip, *Science*, 2011, **333**, 712.
5. D. Zarzo and D. Prats, *Desalination*, 2018, **427**, 1-9.
6. J. Kim, K. Park, D. R. Yang and S. Hong, *Appl. Energy*, 2019, **254**, 113652.
7. S. Lattemann and T. Höpner, *Desalination*, 2008, **220**, 1-15.
8. P. Tao, G. Ni, C. Song, W. Shang, J. Wu, J. Zhu, G. Chen and T. Deng, *Nat. Energy*, 2018, **3**, 1031-1041.
9. O. Neumann, A. S. Urban, J. Day, S. Lal, P. Nordlander and N. J. Halas, *ACS Nano*, 2013, **7**, 42-49.
10. J. Zhou, Y. Gu, P. Liu, P. Wang, L. Miao, J. Liu, A. Wei, X. Mu, J. Li and J. Zhu, *Adv. Funct. Mater.*, 2019, **29**, 1903255.
11. P. Mu, Z. Zhang, W. Bai, J. He, H. Sun, Z. Zhu, W. Liang and A. Li, *Adv. Energy Mater.*, 2019, **9**, 1802158.
12. G. Chen, N. Zhang, N. Li, L. Yu and X. Xu, *Adv. Mater. Interfaces*, 2020, **7**, 1901715.
13. Z. Xu, L. Zhang, L. Zhao, B. Li, B. Bhatia, C. Wang, K. L. Wilke, Y. Song, O. Labban, J. H. Lienhard, R. Wang and E. N. Wang, *Energy Environ. Sci.*, 2020, **13**, 830-839.
14. G. Ni, S. H. Zandavi, S. M. Javid, S. V. Boriskina, T. A. Cooper and G. Chen, *Energy Environ. Sci.*, 2018, **11**, 1510-1519.
15. F. Ni, P. Xiao, C. Zhang, Y. Liang, J. Gu, L. Zhang and T. Chen, *ACS Appl. Mater. Interfaces*, 2019, **11**, 15498-15506.
16. Y. Shi, R. Li, Y. Jin, S. Zhuo, L. Shi, J. Chang, S. Hong, K.-C. Ng and P. Wang, *Joule*, 2018, **2**, 1171-1186.
17. Y. Xia, Q. Hou, H. Jubaer, Y. Li, Y. Kang, S. Yuan, H. Liu, M. W. Woo, L. Zhang, L. Gao, H. Wang and X. Zhang, *Energy Environ. Sci.*, 2019, **12**, 1840-1847.
18. Y. Kuang, C. Chen, S. He, E. M. Hitz, Y. Wang, W. Gan, R. Mi and L. Hu, *Adv. Mater.*, 2019, **31**, 1900498.
19. Y. Guo, X. Zhou, F. Zhao, J. Bae, B. Rosenberger and G. Yu, *ACS Nano*, 2019, **13**, 7913-7919.
20. F. Liu, B. Zhao, W. Wu, H. Yang, Y. Ning, Y. Lai and R. Bradley, *Adv. Funct. Mater.*, 2018, **28**, 1803266.
21. R. Bhardwaj, M. V. ten Kortenaar and R. F. Mudde, *Desalination*, 2013, **326**, 37-45.
22. R. Bhardwaj, M. V. ten Kortenaar and R. F. Mudde, *Appl. Energy*, 2015, **154**, 480-490.
23. F. Zhao, X. Zhou, Y. Shi, X. Qian, M. Alexander, X. Zhao, S. Mendez, R. Yang, L. Qu and G. Yu, *Nat. Nanotechnol.*, 2018, **13**, 489-495.
24. G. Ni, G. Li, Svetlana V. Boriskina, H. Li, W. Yang, T. Zhang and G. Chen, *Nat. Energy*, 2016, **1**, 16126.
25. Y. Guo, F. Zhao, X. Zhou, Z. Chen and G. Yu, *Nano Lett.*, 2019, **19**, 2530-2536.
26. E. Chiavazzo, M. Morciano, F. Viglino, M. Fasano and P. Asinari, *Nat. Sustainability*, 2018, **1**, 763-772.
27. Y. Li, T. Gao, Z. Yang, C. Chen, Y. Kuang, J. Song, C. Jia, E. M. Hitz, B. Yang and L. Hu, *Nano Energy*, 2017, **41**, 201-209.
28. S. He, C. Chen, Y. Kuang, R. Mi, Y. Liu, Y. Pei, W. Kong, W. Gan, H. Xie, E. Hitz, C. Jia, X. Chen, A. Gong, J. Liao, J. Li, Z. J. Ren, B. Yang, S. Das and L. Hu, *Energy Environ. Sci.*, 2019, **12**, 1558-1567.
29. L. Wu, Z. Dong, Z. Cai, T. Ganapathy, N. X. Fang, C. Li, C. Yu, Y. Zhang and Y. Song, *Nat. Commun.*, 2020, **11**, 521.
30. L. Zhu, M. Gao, C. K. N. Peh and G. W. Ho, *Mater. Horiz.*, 2018, **5**, 323-343.
31. M. Gao, L. Zhu, C. K. Peh and G. W. Ho, *Energy Environ. Sci.*, 2019, **12**, 841-864.
32. V.-D. Dao and H.-S. Choi, *Global Challenges*, 2018, **2**, 1700094.
33. C. Zhang, H.-Q. Liang, Z.-K. Xu and Z. Wang, *Adv. Sci.*, 2019, **6**, 1900883.
34. H. Liu, Z. Huang, K. Liu, X. Hu and J. Zhou, *Adv. Energy Mater.*, 2019, **9**, 1900310.
35. Y. Lin, H. Xu, X. Shan, Y. Di, A. Zhao, Y. Hu and Z. Gan, *J. Mater. Chem. A*, 2019, **7**, 19203-19227.
36. S. Cao, Q. Jiang, X. Wu, D. Ghim, H. Gholami Derami, P.-I. Chou, Y.-S. Jun and S. Singamaneni, *J. Mater. Chem. A*, 2019, **7**, 24092-24123.

37. ASTM G173-03(2012), *Standard tables for reference solar spectral irradiances: direct normal and hemispherical on 37° tilted surface*, ASTM international, West Conshohocken, PA, 2012.
38. J. Zhao, Y. Yang, C. Yang, Y. Tian, Y. Han, J. Liu, X. Yin and W. Que, *J. Mater. Chem. A*, 2018, **6**, 16196-16204.
39. X. Yang, Y. Yang, L. Fu, M. Zou, Z. Li, A. Cao and Q. Yuan, *Adv. Funct. Mater.* 2018, **28**, 1704505.
40. X. Zhou, F. Zhao, Y. Guo, Y. Zhang and G. Yu, *Energy Environ. Sci.*, 2018, **11**, 1985-1992.
41. K.-K. Liu, Q. Jiang, S. Tadepalli, R. Raliya, P. Biswas, R. R. Naik and S. Singamaneni, *ACS Appl. Mater. Interfaces*, 2017, **9**, 7675-7681.
42. F. P. Incropera, A. S. Lavine, T. L. Bergman and D. P. DeWitt, *Fundamentals of heat and mass transfer*, Wiley, 2007.
43. Y. Yang, H. Zhao, Z. Yin, J. Zhao, X. Yin, N. Li, D. Yin, Y. Li, B. Lei, Y. Du and W. Que, *Mater. Horiz.*, 2018, **5**, 1143-1150.
44. G. Ni, G. Li, Svetlana V. Boriskina, H. Li, W. Yang, T. Zhang and G. Chen, *Nat. Energy*, 2016, **1**, 16126.
45. C. Finnerty, L. Zhang, D. L. Sedlak, K. L. Nelson and B. Mi, *Environ. sci. technol.* 2017, **51**, 11701-11709.
46. P. Zhang, J. Li, L. Lv, Y. Zhao and L. Qu, *ACS Nano*, 2017, **11**, 5087-5093.
47. K. M. S. Eldalil, *Desalination*, 2010, **251**, 3-11.
48. Z. M. Omara, A. S. Abdullah, A. E. Kabeel and F. A. Essa, *Renewable and Sustainable Energy Rev.*, 2017, **78**, 176-193.
49. V. Dimri, B. Sarkar, U. Singh and G. N. Tiwari, *Desalination*, 2008, **227**, 178-189.
50. M. Gao, P. K. N. Connor and G. W. Ho, *Energy Environ. Sci.*, 2016, **9**, 3151-3160.
51. D. P. Storer, J. L. Phelps, X. Wu, G. Owens, N. I. Khan and H. Xu, *ACS Appl. Mater. Interfaces*, 2020, **12**, 15279-15287.
52. K. Bae, G. Kang, S. K. Cho, W. Park, K. Kim and W. J. Padilla, *Nat. Commun.*, 2015, **6**, 10103.
53. Z. Wang, Y. Liu, P. Tao, Q. Shen, N. Yi, F. Zhang, Q. Liu, C. Song, D. Zhang, W. Shang and T. Deng, *Small*, 2014, **10**, 3234-3239.
54. Z. Huang, S. Li, X. Cui, Y. Wan, Y. Xiao, S. Tian, H. Wang, X. Li, Q. Zhao and C.-S. Lee, *J. Mater. Chem. A*, 2020, DOI: 10.1039/D0TA01980A.
55. L. Zhou, Y. Tan, D. Ji, B. Zhu, P. Zhang, J. Xu, Q. Gan, Z. Yu and J. Zhu, *Sci. Adv.*, 2016, **2**, e1501227.
56. J. Li, X. Wang, Z. Lin, N. Xu, X. Li, J. Liang, W. Zhao, R. Lin, B. Zhu, G. Liu, L. Zhou, S. Zhu and J. Zhu, *Joule*, 2020, **4**, 928-937.
57. B. Zhang, C. Song, C. Liu, J. Min, J. Azadmanjiri, Y. Ni, R. Niu, J. Gong, Q. Zhao and T. Tang, *J. Mater. Chem. A*, 2019, **7**, 22912-22923.
58. C. Song, L. Hao, B. Zhang, Z. Dong, Q. Tang, J. Min, Q. Zhao, R. Niu, J. Gong and T. Tang, *Sci. China Mater.* 2020, **63**, 779-793.
59. N. Liu, L. Hao, B. Zhang, R. Niu, J. Gong and T. Tang, *Sustainable Energy Fuels*, 2020, DOI: 10.1039/D0SE01239D.
60. Q. Hou, C. Xue, N. Li, H. Wang, Q. Chang, H. Liu, J. Yang and S. Hu, *Carbon*, 2019, **149**, 556-563.
61. A. Celzard, A. Pasc, S. Schaefer, K. Mandel, T. Ballweg, S. Li, G. Medjahdi, V. Nicolas and V. Fierro, *Carbon*, 2019, **146**, 232-247.
62. M. Zhu, Y. Li, F. Chen, X. Zhu, J. Dai, Y. Li, Z. Yang, X. Yan, J. Song, Y. Wang, E. Hitz, W. Luo, M. Lu, B. Yang and L. Hu, *Adv. Energy Mater.*, 2018, **8**, 1701028.
63. I. Ihsanullah, *Nano-Micro Lett.*, 2020, **12**, 72.
64. X. Zhao, X.-J. Zha, J.-H. Pu, L. Bai, R.-Y. Bao, Z.-Y. Liu, M.-B. Yang and W. Yang, *J. Mater. Chem. A*, 2019, **7**, 10446-10455.
65. L. Su, Y. Hu, Z. Ma, L. Miao, J. Zhou, Y. Ning, Z. Chang, B. Wu, M. Cao, R. Xia and J. Qian, *Sol. Energy Mater. Sol. Cells*, 2020, **210**, 110484.
66. H. Zhang, Y. Wang, Y. Liu, M. Zhao, C. Liu, Y. Wang, M. K. Albolokany, N. Wu, M. Wang, L. Yang and B. Liu, *ChemSusChem*, 2020, **n/a**.
67. J. Wang, Y. Li, L. Deng, N. Wei, Y. Weng, S. Dong, D. Qi, J. Qiu, X. Chen and T. Wu, *Adv. Mater.*, 2017, **29**, 1603730.
68. T. Li, Q. Fang, H. Lin and F. Liu, *J. Mater. Chem. A*, 2019, **7**, 17505-17515.
69. Y. Li, T. Gao, Z. Yang, C. Chen, W. Luo, J. Song, E. Hitz, C. Jia, Y. Zhou, B. Liu, B. Yang and L. Hu, *Adv. Mater.*, 2017, **29**, 1700981.
70. X. Zhao and C. Liu, *Sol. Energy*, 2020, **195**, 304-309.
71. F. Zhao, Y. Guo, X. Zhou, W. Shi and G. Yu, *Nat. Rev. Mater.*, 2020, **5**, 388-401.
72. Q. Zhu, K. Ye, W. Zhu, W. Xu, C. Zou, L. Song, E. Sharman, L. Wang, S. Jin, G. Zhang, Y. Luo and J. Jiang, *J. Phys. Chem. Lett.*, 2020, **11**, 2502-2509.
73. M. Chen, Y. Wu, W. Song, Y. Mo, X. Lin, Q. He and B. Guo, *Nanoscale*, 2018, **10**, 6186-6193.
74. S. Gao, X. Dong, J. Huang, J. Dong, F. D. Maggio, S. Wang, F. Guo, T. Zhu, Z. Chen and Y. Lai, *Global Challenges*, 2019, **3**, 1800117.
75. Y. Xu, J. Ma, D. Liu, H. Xu, F. Cui and W. Wang, *Chem. Eng. J.*, 2019, **356**, 869-876.
76. Y. Wang, C. Wang, X. Song, M. Huang, S. K. Megarajan, S. F. Shaikat and H. Jiang, *J. Mater. Chem. A*, 2018, **6**, 9874-9881.
77. W. Li, Z. Li, K. Bertelsmann and D. E. Fan, *Adv. Mater.*, 2019, **31**, 1900720.
78. S. Hong, Y. Shi, R. Li, C. Zhang, Y. Jin and P. Wang, *ACS Appl. Mater. Interfaces*, 2018, **10**, 28517-28524.
79. P. Sun, W. Zhang, I. Zada, Y. Zhang, J. Gu, Q. Liu, H. Su, D. Pantelić, B. Jelenković and D. Zhang, *ACS Appl. Mater. Interfaces*, 2020, **12**, 2171-2179.
80. X. Li, R. Lin, G. Ni, N. Xu, X. Hu, B. Zhu, G. Lv, J. Li, S. Zhu and J. Zhu, *Natl. Sci. Rev.*, 2017, **5**, 70-77.
81. Y. Bian, Y. Shen, K. Tang, Q. Du, L. Hao, D. Liu, J. Hao, D. Zhou, X. Wang, H. Zhang, P. Li, Y. Sang, X. Yuan, L. Zhao, J. Ye, B. Liu, H. Lu, Y. Yang, R. Zhang, Y. Zheng, X. Xiong

- and S. Gu, *Global Challenges*, 2019, **3**, 1900040.
82. X. Qian, Y. Zhao, Y. Alsaid, X. Wang, M. Hua, T. Galy, H. Gopalakrishna, Y. Yang, J. Cui, N. Liu, M. Marszewski, L. Pilon, H. Jiang and X. He, *Nat. Nanotechnol.*, 2019, **14**, 1048-1055.
  83. L. A. Weinstein, J. Loomis, B. Bhatia, D. M. Bierman, E. N. Wang and G. Chen, *Chem. Rev.*, 2015, **115**, 12797-12838.
  84. Q. Yang, C. Xu, F. Wang, Z. Ling, Z. Zhang and X. Fang, *ACS Appl. Energy Mater.*, 2019, **2**, 7223-7232.
  85. H. Song, Y. Liu, Z. Liu, M. H. Singer, C. Li, A. R. Cheney, D. Ji, L. Zhou, N. Zhang, X. Zeng, Z. Bei, Z. Yu, S. Jiang and Q. Gan, *Adv. Sci.*, 2018, **5**, 1800222.
  86. X. Li, J. Li, J. Lu, N. Xu, C. Chen, X. Min, B. Zhu, H. Li, L. Zhou, S. Zhu, T. Zhang and J. Zhu, *Joule*, 2018, **2**, 1331-1338.
  87. C. Tu, W. Cai, X. Chen, X. Ouyang, H. Zhang and Z. Zhang, *Small*, 2019, **15**, 1902070.
  88. X. Zhou, Y. Guo, F. Zhao and G. Yu, *Acc. Chem. Res.*, 2019, **52**, 3244-3253.
  89. X. Zhou, F. Zhao, Y. Guo, B. Rosenberger and G. Yu, *Sci. Adv.*, 2019, **5**, eaaw5484.
  90. J. Tang, T. Zheng, Z. Song, Y. Shao, N. Li, K. Jia, Y. Tian, Q. Song, H. Liu and G. Xue, *ACS Appl. Mater. Interfaces*, 2020, **12**, 18504-18511.
  91. N. Xu, J. Li, Y. Wang, C. Fang, X. Li, Y. Wang, L. Zhou, B. Zhu, Z. Wu, S. Zhu and J. Zhu, *Sci. Adv.*, 2019, **5**, eaaw7013.
  92. J. Liu, Q. Liu, D. Ma, Y. Yuan, J. Yao, W. Zhang, H. Su, Y. Su, J. Gu and D. Zhang, *J. Mater. Chem. A*, 2019, **7**, 9034-9039.
  93. Z. Li, J. Zhang, S. Zang, C. Yang, Y. Liu, F. Jing, H. Jing, J. Hu, C. Wang and Y. Zhou, *Nano Energy*, 2020, **73**, 104834.
  94. X. Wang, Q. Gan, R. Chen, H. Peng, T. Zhang and M. Ye, *ACS Sustainable Chem. Eng.*, 2020, DOI: 10.1021/acssuschemeng.9b06844.
  95. Y. Shi, C. Zhang, R. Li, S. Zhuo, Y. Jin, L. Shi, S. Hong, J. Chang, C. Ong and P. Wang, *Environ. Sci. Technol.* 2018, **52**, 11822-11830.
  96. X. Meng, J. Yang, S. Ramakrishna, Y. Sun and Y. Dai, *ACS Sustainable Chem. Eng.*, 2020, **8**, 4955-4965.
  97. C. Liu, C. Cai and X. Zhao, *ACS Sustainable Chem. Eng.*, 2020, **8**, 1548-1554.
  98. Y. Yang, Y. Sui, Z. Cai and B. Xu, *Global Challenges*, 2019, **3**, 1900004.
  99. Q. Chen, Z. Pei, Y. Xu, Z. Li, Y. Yang, Y. Wei and Y. Ji, *Chem. Sci.*, 2018, **9**, 623-628.
  100. L. Zhu, M. Gao, C. K. N. Peh, X. Wang and G. W. Ho, *Adv. Energy Mater.*, 2018, **8**, 1702149.
  101. C. Xiao, W. Liang, L. Chen, J. He, F. Liu, H. Sun, Z. Zhu and A. Li, *ACS Appl. Energy Mater.*, 2019, **2**, 8862-8870.
  102. L. Yang, G. Chen, N. Zhang, Y. Xu and X. Xu, *ACS Sustainable Chem. Eng.*, 2019, **7**, 19311-19320.
  103. Y. Yang, X. Yang, L. Fu, M. Zou, A. Cao, Y. Du, Q. Yuan and C.-H. Yan, *ACS Energy Lett.*, 2018, **3**, 1165-1171.
  104. N. Xu, X. Hu, W. Xu, X. Li, L. Zhou, S. Zhu and J. Zhu, *Adv. Mater.*, 2017, **29**, 1606762. DOI: 10.1039/D0TA08869B
  105. X. Hu, W. Xu, L. Zhou, Y. Tan, Y. Wang, S. Zhu and J. Zhu, *Adv. Mater.*, 2017, **29**, 1604031.
  106. C. Chen, Y. Li, J. Song, Z. Yang, Y. Kuang, E. Hitz, C. Jia, A. Gong, F. Jiang, J. Y. Zhu, B. Yang, J. Xie and L. Hu, *Adv. Mater.*, 2017, **29**, 1701756.
  107. W. Xu, Y. Xing, J. Liu, H. Wu, Y. Cui, D. Li, D. Guo, C. Li, A. Liu and H. Bai, *ACS Nano*, 2019, **13**, 7930-7938.
  108. W. Huang, P. Su, Y. Cao, C. Li, D. Chen, X. Tian, Y. Su, B. Qiao, J. Tu and X. Wang, *Nano Energy*, 2020, **69**, 104465.
  109. Z. Yu, S. Cheng, C. Li, L. Li and J. Yang, *ACS Appl. Mater. Interfaces*, 2019, **11**, 32038-32045.
  110. Q. Ma, P. Yin, M. Zhao, Z. Luo, Y. Huang, Q. He, Y. Yu, Z. Liu, Z. Hu, B. Chen and H. Zhang, *Adv. Mater.*, 2019, **31**, 1808249.
  111. H. Ren, M. Tang, B. Guan, K. Wang, J. Yang, F. Wang, M. Wang, J. Shan, Z. Chen, D. Wei, H. Peng and Z. Liu, *Adv. Mater.*, 2017, **29**, 1702590.
  112. Y. Zhang, T. Xiong, D. K. Nandakumar and S. C. Tan, *Adv. Sci.*, 2020, **7**, 1903478.
  113. F. Wang, D. Wei, Y. Li, T. Chen, P. Mu, H. Sun, Z. Zhu, W. Liang and A. Li, *J. Mater. Chem. A*, 2019, **7**, 18311-18317.
  114. W. Xu, X. Hu, S. Zhuang, Y. Wang, X. Li, L. Zhou, S. Zhu and J. Zhu, *Adv. Energy Mater.*, 2018, **8**, 1702884.
  115. Q. Zhang, G. Yi, Z. Fu, H. Yu, S. Chen and X. Quan, *ACS Nano*, 2019, **13**, 13196-13207.
  116. C.-S. Hu, H.-J. Li, J.-Y. Wang, A. Haleem, X.-C. Li, M. Siddiq and W.-D. He, *ACS Appl. Energy Mater.*, 2019, **2**, 7554-7563.
  117. Y. Pang, J. Zhang, R. Ma, Z. Qu, E. Lee and T. Luo, *ACS Energy Lett.*, 2020, **5**, 437-456.
  118. W. Zhang, G. Zhang, Q. Ji, H. Liu, R. Liu and J. Qu, *ACS Appl. Mater. Interfaces*, 2019, **11**, 9974-9983.
  119. D. Hao, Y. Yang, B. Xu and Z. Cai, *ACS Sustainable Chem. Eng.*, 2018, **6**, 10789-10797.
  120. S.-L. Loo, L. Vásquez, U. C. Paul, L. Campagnolo, A. Athanassiou and D. Fragouli, *ACS Appl. Mater. Interfaces*, 2020, **12**, 10307-10316.
  121. Q. Fang, T. Li, Z. Chen, H. Lin, P. Wang and F. Liu, *ACS Appl. Mater. Interfaces*, 2019, **11**, 10672-10679.
  122. L. Zhao, C. Du, C. Zhou, S. Sun, Y. Jia, J. Yuan, G. Song, X. Zhou, Q. Zhao and S. Yang, *ACS Sustainable Chem. Eng.*, 2020, **8**, 4362-4370.
  123. L. Noureen, Z. Xie, Y. Gao, M. Li, M. Hussain, K. Wang, L. Zhang and J. Zhu, *ACS Appl. Mater. Interfaces*, 2020, **12**, 6343-6350.
  124. P. Zhang, Q. Liao, H. Yao, H. Cheng, Y. Huang, C. Yang, L. Jiang and L. Qu, *J. Mater. Chem. A*, 2018, **6**, 15303-15309.
  125. Y. Xu, C. Tang, J. Ma, D. Liu, D. Qi, S. You, F. Cui, Y. Wei and W. Wang, *Environ. Sci. Technol.*, 2020, **54**, 5150-5158.
  126. Q. Zhang, H. Yang, X. Xiao, H. Wang, L. Yan, Z. Shi, Y. Chen, W. Xu and X. Wang, *J. Mater. Chem. A*, 2019, **7**, 14620-14628.



127. P. Zhang, Q. Liao, T. Zhang, H. Cheng, Y. Huang, C. Yang, C. Li, L. Jiang and L. Qu, *Nano Energy*, 2018, **46**, 415-422.
128. H. Li, H. Wen, J. Li, J. Huang, D. Wang and B. Z. Tang, *ACS Appl. Mater. Interfaces*, 2020, **12**, 26033-26040.
129. G. Xue, Q. Chen, S. Lin, J. Duan, P. Yang, K. Liu, J. Li and J. Zhou, *Global Challenges*, 2018, **2**, 1800001.
130. M. K. Phadatare and S. K. Verma, *Desalin. Water Treat.*, 2009, **2**, 254-259.
131. P. Zanganeh, A. S. Goharizi, S. Ayatollahi and M. Feilizadeh, *J. Cleaner Prod.*, 2020, **265**, 121758.
132. K. Zhu and L. Pilon, *J. Quant. Spectrosc. Radiat. Transfer*, 2017, **201**, 53-63.
133. B. Janarthanan, J. Chandrasekaran and S. Kumar, *Desalination*, 2006, **190**, 51-62.
134. B. A. K. Abu-Hijleh and H. A. Mousa, *Energy*, 1997, **22**, 43-48.
135. P. U. Suneesh, R. Jayaprakash, T. Arunkumar and D. Denkenberger, *Desalination*, 2014, **337**, 1-5.
136. L. Zhang, B. Tang, J. Wu, R. Li and P. Wang, *Adv. Mater.*, 2015, **27**, 4889-4894.
137. Z. Wang, T. Horseman, A. P. Straub, N. Y. Yip, D. Li, M. Elimelech and S. Lin, *Sci. adv.*, 2019, **5**, eaax0763-eaax0763.
138. B. Zhu, H. Kou, Z. Liu, Z. Wang, D. K. Macharia, M. Zhu, B. Wu, X. Liu and Z. Chen, *ACS Appl. Mater. Interfaces*, 2019, **11**, 35005-35014.
139. X. Wang, G. Ou, N. Wang and H. Wu, *ACS Appl. Mater. Interfaces*, 2016, **8**, 9194-9199.
140. C. Xing, D. Huang, S. Chen, Q. Huang, C. Zhou, Z. Peng, J. Li, X. Zhu, Y. Liu, Z. Liu, H. Chen, J. Zhao, J. Li, L. Liu, F. Cheng, D. Fan and H. Zhang, *Adv. Sci.*, 2019, **6**, 1900531.
141. P. Qiao, J. Wu, H. Li, Y. Xu, L. Ren, K. Lin and W. Zhou, *ACS Appl. Mater. Interfaces*, 2019, **11**, 7066-7073.
142. A. K. Menon, I. Haechler, S. Kaur, S. Lubner and R. S. Prasher, *Nat. Sustainability*, 2020, **3**, 144-151.
143. Y. Qin, Y. Wang, X. Sun, Y. Li, H. Xu, Y. Tan, Y. Li, T. Song and B. Sun, *Angew. Chem. Int. Ed.*, 2020, **n/a**.
144. G. Li, W.-C. Law and K. C. Chan, *Green Chem.*, 2018, **20**, 3689-3695.
145. X. Wang, Q. Liu, S. Wu, B. Xu and H. Xu, *Adv. Mater.*, 2019, **31**, 1807716.
146. Q. Zhao, C. Du, Y. Jia, J. Yuan, G. Song, X. Zhou, S. Sun, C. Zhou, L. Zhao and S. Yang, *Chem. Eng. J.*, 2020, **387**, 124131.
147. K. Sampathkumar, T. V. Arjunan, P. Pitchandi and P. Senthilkumar, *Renewable Sustainable Energy Rev.*, 2010, **14**, 1503-1526.
148. Z. Deng, J. Zhou, L. Miao, C. Liu, Y. Peng, L. Sun and S. Tanemura, *J. Mater. Chem. A*, 2017, **5**, 7691-7709.
149. M. S. Zielinski, J.-W. Choi, T. La Grange, M. Modestino, S. M. H. Hashemi, Y. Pu, S. Birkhold, J. A. Hubbell and D. Psaltis, *Nano Lett.*, 2016, **16**, 2159-2167.
150. S. Ishii, R. P. Sugavaneshwar and T. Nagao, *J. Phys. Chem. C*, 2016, **120**, 2343-2348.
151. L. Zhou, Y. Tan, J. Wang, W. Xu, Y. Yuan, W. Cai, S. Zhu and J. Zhu, *Nat. Photonics*, 2016, **10**, 393-398.
152. Q. Wang, Z. Zhu, G. Wu, X. Zhang and H. Zheng, *ACS Appl. Energy*, 2018, **224**, 510-526.
153. J. Lou, Y. Liu, Z. Wang, D. Zhao, C. Song, J. Wu, N. Dasgupta, W. Zhang, D. Zhang, P. Tao, W. Shang and T. Deng, *ACS Appl. Mater. Interfaces*, 2016, **8**, 14628-14636.
154. X. Liu, H. Liu, X. Yu, L. Zhou and J. Zhu, *Curr. Opin. Chem. Eng.*, 2019, **25**, 26-34.
155. Y. Li, X. Cui, M. Zhao, Y. Xu, L. Chen, Z. Cao, S. Yang and Y. Wang, *J. Mater. Chem. A*, 2019, **7**, 704-710.
156. M. Gao, C. K. Peh, H. T. Phan, L. Zhu and G. W. Ho, *Adv. Energy Mater.*, 2018, **8**, 1800711.
157. G. Liu, T. Chen, J. Xu, G. Li and K. Wang, *J. Mater. Chem. A*, 2020, **8**, 513-531.
158. P. Yang, K. Liu, Q. Chen, J. Li, J. Duan, G. Xue, Z. Xu, W. Xie and J. Zhou, *Energy Environ. Sci.*, 2017, **10**, 1923-1927.
159. W. Xu, X. Zhou, C. Hao, H. Zheng, Y. Liu, X. Yan, Z. Yang, M. Leung, X. C. Zeng, R. X. Xu and Z. Wang, *Natl. Sci. Rev.*, 2019, **6**, 540-550.
160. P. Xiao, J. He, F. Ni, C. Zhang, Y. Liang, W. Zhou, J. Gu, J. Xia, S.-W. Kuo and T. Chen, *Nano Energy*, 2020, **68**, 104385.
161. X. Li, X. Min, J. Li, N. Xu, P. Zhu, B. Zhu, S. Zhu and J. Zhu, *Joule*, 2018, **2**, 2477-2484.
162. L. Zhu, T. Ding, M. Gao, C. K. N. Peh and G. W. Ho, *Adv. Energy Mater.*, 2019, **9**, 1900250.
163. G. Xue, Y. Xu, T. Ding, J. Li, J. Yin, W. Fei, Y. Cao, J. Yu, L. Yuan, L. Gong, J. Chen, S. Deng, J. Zhou and W. Guo, *Nat. Nanotechnol.*, 2017, **12**, 317-321.

View Article Online  
DOI: 10.1039/C9JA00189A